Available online at www.sciencedirect.com
ScienceDirect
Geochimica et Cosmochimica Acta 73 (2009) 4180–4198
Geochimica et Cosmochimica Acta
www.elsevier.com/locate/gca

Precipitation of amorphous $CaCO_3$ (aragonite-like) by cyanobacteria: A STXM study of the influence of EPS on the nucleation process

M. Obst [a,b,*,1], J.J. Dynes [b,c], J.R. Lawrence [c], G.D.W. Swerhone [c], K. Benzerara [d], C. Karunakaran [a], K. Kaznatcheev [a], T. Tyliszczak [e], A.P. Hitchcock [b]

[a] *Canadian Light Source, 101 Perimeter Road, Saskatoon, Sask., Canada S7H 0X4*
[b] *BIMR, McMaster University Hamilton, Ont., Canada L8S 4M1*
[c] *Environment Canada, Saskatoon, Sask., Canada S7N 3H5*
[d] *IMPMC, ULR 7590, CNRS & IPGP, Paris, France*
[e] *Advanced Light Source, Lawrence Berkeley National Laboratory, Berkeley, CA 94720, USA*

Received 10 October 2008; accepted in revised form 13 April 2009; available online 24 April 2009

Abstract

An amorphous or nanocrystalline calcium carbonate (ACC) phase with aragonite-like short-range order was found to be a transient precursor phase of calcite precipitation mediated by cyanobacteria of the strain *Synechococcus leopoliensis* PCC 7942. Using scanning transmission X-ray microscopy (STXM), different Ca-species such as calcite, aragonite-like $CaCO_3$, and Ca adsorbed on extracellular polymers were discriminated and mapped, together with various organic compounds, at the 30 nm-scale. The nucleation of the amorphous aragonite-like $CaCO_3$ was found to take place within the tightly bound extracellular polymeric substances (EPS) produced by the cyanobacteria very close to the cell wall. The aragonite-like $CaCO_3$ is a type of ACC since it did not show either X-ray or electron diffraction peaks. The amount of aragonite-like $CaCO_3$ precipitated in the EPS was dependent on the nutrient supply during bacterial growth. Higher nutrient concentrations (both N and P) during the cultivation of the cyanobacteria resulted in higher amounts of precipitation of the aragonite-like $CaCO_3$, whereas the amount of Ca^{2+} adsorbed per volume of EPS was almost independent of the nutrient level. After the onset of the precipitation of the thermodynamically stable calcite and loss of supersaturation the aragonite-like $CaCO_3$ dissolved whereas Ca^{2+} remained sorbed to the EPS albeit at lower concentrations. Based on these observations a model describing the temporal and spatial evolution of calcite nucleation on the surface of *S. leopoliensis* was developed. In another set of STXM experiments the amount of aragonite-like $CaCO_3$ precipitated on the cell surface was found to depend on the culture growth phase: cells in the exponential growth phase adsorbed large amounts of Ca within the EPS and mediated nucleation of ACC, while cells at the stationary/death phase neither adsorbed large amounts of Ca^{2+} nor mediated the formation of aragonite-like $CaCO_3$. It is suggested that precipitation of an X-ray amorphous $CaCO_3$ layer by cyanobacteria could serve as a protection mechanism against uncontrolled precipitation of a thermodynamically stable phase calcite on their surface.

1. INTRODUCTION

Freshwater cyanobacterial calcification has been proposed as a major contributor to the formation of carbonate deposits (Thompson and Ferris, 1990). The mechanisms of carbonate nucleation and growth are however not yet fully understood. In a laboratory approach that mimics

* Corresponding author.
E-mail address: obst@gmx.ch (M. Obst).
[1] Present address: Center for Applied Geoscience, Eberhard-Karls University Tuebingen, Sigwartstrasse 10, 72076 Tuebingen, Germany.

0016-7037/$ - see front matter © 2009 Elsevier Ltd. All rights reserved.
doi:10.1016/j.gca.2009.04.013

freshwater systems supersaturated with respect to calcite, this study focuses on the mechanisms of $CaCO_3$ nucleation by a freshwater cyanobacterial strain *Synechococcus leopoliensis* PCC 7942.

Cyanobacteria are ubiquitous and abundant particularly under oligotrophic conditions, where they are a major contributor to total primary production (Weisse, 1993). Specifically cyanobacteria of the genus *Synechococcus* are very common in freshwater environments and are the most abundant genus in some hardwater lakes (Schultze-Lam et al., 1992). Most of these environments are at least temporarily supersaturated with respect to $CaCO_3$ mineral phases such as calcite and the resulting precipitation of calcite from hardwater lakes is a phenomenon that has been studied for decades (for an overview see Küchler-Krischun and Kleiner, 1990). The chemical microenvironment of cyanobacteria is diffusion controlled (Beveridge, 1988), and therefore it seems that cyanobacteria influence the conditions in their microenvironment by the photosynthetic uptake of CO_2 or HCO_3^-, particularly when diffusion is limited by dense extracellular polymers (EPS) such as in cyanobacterial mats (Pentecost, 1991; Merz-Preiss, 2000). Cyanobacterial calcification can be promoted by carbon concentrating mechanisms resulting in a rise of pH in the microenvironment of the cells, which leads to significant $CaCO_3$ supersaturation within the sheath of filamentous cyanobacteria, followed by $CaCO_3$ precipitation (Kah and Riding, 2007). Another mechanism, which might play a role for the adsorption of calcium to the cell surface as a first step of $CaCO_3$ precipitation particularly under more alkaline conditions, is an active influence of the metabolism of cyanobacteria on their surface potential which the cells might use to facilitate the uptake of inorganic carbon under alkaline conditions (Martinez et al., 2008).

However, the influence of the organism is only one aspect of the calcification process. Although cyanobacteria influence their chemical microenvironments in biofilms, Golubic (1973) reported that cyanobacterial calcification strongly depends on environmental conditions. This environmental influence was confirmed by Riding (1992) and Arp et al. (2001) who stated that calcification is not obligate amongst cyanobacteria but dependent on conditions favoring calcification. Merz (1992) reported that cyanobacterial calcification only occurs in $CaCO_3$ supersaturated waters and that only certain genera calcify, but none of them are obligate calcifiers. There is reduced diffusion in biofilms and bacterial mats which results in a higher influence of biofilm forming cyanobacteria on their chemical microenvironment as compared to planktonic species. This suggests that planktonic cyanobacterial calcification will be influenced by the aqueous environment of the cells to an even higher degree than biofilm cyanobacteria.

Moreover, photoautotrophic planktonic species in lakes require buoyancy in order to stay within the euphotic zone. The uncontrolled precipitation of carbonates attached to their cell surface would reduce their buoyancy, causing the cyanobacteria to sink below the euphotic zone, thus resulting in their death. In that view, the uncontrolled precipitation of calcite by cyanobacteria would be deleterious and simply could result from catastrophic changes in environmental conditions such as pH caused by the photosynthetic uptake of CO_2.

In contrast, Merz (1992) proposed two potential benefits of $CaCO_3$ precipitation to the cyanobacteria: Firstly, the precipitation of $CaCO_3$ could be a mechanism to protect the cells from high light intensities which damage the photosynthetic apparatus, particularly for cyanobacteria living in shallow waters or high altitudes. Secondly, the precipitation can act as an ion sink which buffers the rise of pH in the cells' microenvironment due to photosynthesis and therefore allows higher rates of photosynthesis. The details of these biomineralization processes are however still poorly known.

In a bulk biogeochemical approach Obst et al. (in press), previously investigated the nucleation kinetics of calcite mediated by *S. leopoliensis* under chemically well controlled conditions similar to those used in the present study. The authors observed that large calcite crystals only attached to a rather small fraction of the cells. However, they did not observe any indication for biological control of this process or significant influence of the photosynthetic activity on the nucleation kinetics of calcite on the cell surface.

Thus, the precipitation of calcite by *S. leopoliensis* PCC 7942 seemed to be in contrast to controlled precipitation mechanisms whereby the microorganisms control the polymorph of the mineral phase (e.g. by an organic matrix acting as a template for nucleation), such as the composite exoskeleton of coccolithophorids (Young et al., 1999), foraminifera (Erez, 2003) or microbially controlled precipitation of calcium phosphate in the periplasm of *Ramlibacter tataouinensis* (Benzerara et al., 2004a), However, transmission electron microscopy (TEM) observations of biogenic calcite crystals precipitated by *S. leopoliensis* PCC 7942 suggested that some of these crystals nucleated on the cell surface and most likely within a thin layer of EPS, since residues of these polymers were found on the crystal (see e.g. Fig. 3 in Obst et al., 2005), but the function of the EPS, and the benefit of the cyanobacteria from the calcification of a small fraction of the cells remained unclear.

Using synchrotron-based soft X-ray spectromicroscopy, in the present study the early stages of the $CaCO_3$ precipitation were investigated in order to better understand the associations of the different reactive surfaces such as the cell membranes and EPS with the different Ca-species that were present in the solutions. Based on a model developed in a previous study of Obst et al. (in press), the average induction times of calcite nucleation for a given supersaturation were determined and supersaturated cell suspensions were sampled close to these induction periods. Special attention was paid to the structure, crystallinity and homogeneity of the first precipitates. Furthermore we focused on the influence of the EPS produced by *S. leopoliensis,* as extracellular polymers are known to influence the mineralogy and morphology of $CaCO_3$ precipitates in a variety of environments (Kawaguchi and Decho, 2002; Braissant et al., 2003; Braissant et al., 2007).

Early stages of cyanobacterial biomineralization are difficult to investigate because of the small spatial scale involved. Therefore we used soft X-ray scanning transmission X-ray microscopy (STXM), a synchrotron-based spec-

tromicroscopy which combines the speciation capabilities of near edge X-ray absorption fine structure (NEXAFS) spectroscopy with a spatial resolution in the order of <25 nm. STXM does not require sectioning or staining. Monochromatic soft X-rays are absorbed by the sample at specific energies which represent the excitation of core-electrons to unoccupied anti-bonding states. These excited states have energies, intensities and linear dichroic properties characteristic of the chemical species being excited (Stoehr, 1996). Thus, STXM is capable of determining and mapping various species of carbon such as the major biomolecules composing microorganisms, i.e. proteins which have their highest abundance within the microbial cells or polysaccharides which are the major component of EPS (Dynes et al., 2006b), and to identify the Ca-species involved in the nucleation process such as Ca-containing mineral phases (Benzerara et al., 2004b). As a result, we mapped at a spatial resolution of ~30 nm the inorganic species involved in the first steps of cyanobacterial biomineralization processes and relate those to the major biomacromolecules such as protein, polysaccharide and lipid as a function of environmental parameters.

2. MATERIALS AND METHODS

All solutions used in these experiments were prepared from reagent grade chemicals (Sigma–Aldrich, Fluka) and Millipore™ deionized water.

2.1. Cell cultures

Planktonic cyanobacteria of the strain *S. leopoliensis* PCC 7942 were cultured at three different nutrient levels which are referred to as culture medium *Z* (high nutrient concentrations), *Z*/4 (medium) and *Z*/10 (low). These culture media contained 59 mg L^{-1} $Ca(NO_3)_2{\cdot}4H_2O$, 467 mg L^{-1} $NaNO_3$, 41 mg L^{-1} $K_2HPO_4{\cdot}3H_2O$, 25 mg L^{-1} $MgSO_4{\cdot}7H_2O$ or these concentrations divided by 4 or 10, respectively. All media were buffered by 168 mg L^{-1} $NaHCO_3$ and contained 11.5 mg L^{-1} Na–EDTA, 3 mg L^{-1} $FeSO_4{\cdot}7H_2O$, 248 μg L^{-1} H_3BO_3, 135 μg L^{-1} $MnSO_4{\cdot}H_2O$, 7.2 μg L^{-1} $(NH_4)_6Mo_7O_{24}{\cdot}4H_2O$, 23.2 μg L^{-1} $ZnSO_4{\cdot}7H_2O$, 12 μg L^{-1} $Co(NO_3)_2{\cdot}6H_2O$ and 10.4 μg L^{-1} $CuSO_4{\cdot}5H_2O$. No vitamin solution was added. Fluorescent lights provided a permanent light intensity of 4 μE m^{-2} s^{-1}. After the cultures were grown at room temperature (20 ± 2 °C) on a shaker for 25 day (exponential growth phase) and 198 day (stationary growth phase/death phase) periods the cyanobacteria were filtered (pore size 0.2 μm).

2.2. $CaCO_3$ nucleation experiments

The filtered cyanobacteria were then gently re-suspended in $NaHCO_3/CaCl_2$ solutions supersaturated with respect to calcite. For an overview of the experimental conditions and sampling times see Table 1. The saturation state $\Omega = \mathrm{IAP}\ \mathrm{SP}^{-1}$ (where IAP is the ion activity product and SP is the solubility product) and the initial pH were calculated with PhreeqC Interactive (V2.13.2) using the Wateq4F database and assuming equilibrium with 384 ppm atmospheric CO_2. The suspensions were kept under illumination in centrifuge tubes. According to the model of De Yoreo and Vekilov (2003) the induction time of mineral nucleation is proportional to the third power of the saturation index in the argument of an exponential. The sampling times for the two different Ca^{2+} concentrations were then chosen to be close to the induction time of calcite nucleation which were calculated using a model of the induction time based on the measurements of induction times in long-term nucleation experiments (Obst et al., in press).

2.3. Sample preparation for the STXM experiments

To investigate the influence of environmental parameters on mineral nucleation and precipitation mechanisms we used a laboratory approach which allowed us to carefully control the experimental conditions. This allowed us to efficiently analyze the influence of the growth conditions of the bacteria and the culture age, the influence of supersaturation, and the temporal evolution of the precipitation by varying one parameter while keeping the others constant. The acquisition of a full STXM dataset containing image sequences of ~4 × 4 μm^2 areas at the C-1s and the Ca-2p regions, both with approximately 150 energy steps, with fine spatial sampling (40 nm pixel sizes) takes up to 6 h including the sample selection and navigation. Because of the limited time available at state-of-the-art STXM beamlines, only small sample areas could be analyzed which had to be chosen carefully by pre-screening the samples with conventional optical microscopy and STXM mapping as described below. As a first but very important step, we ensured that the analyzed samples were homogeneous and representative. After the Ca-incubation all STXM samples were prepared by deposition of 1–2 μL of the cell suspension onto Si_3N_4 windows (1 × 1 mm, thickness 100 nm on a 200 μm thick Si chip, 5 × 5 mm, Norcada Inc., Edmonton, Canada). The droplet was then slowly moved by gravity across the window area where cells stuck to the surface. When the droplet partially covered the window, the suspension was completely removed by capillary suction using a filter paper in order to prevent precipitation artifacts from drying. The sample was then air-dried within a few seconds under the illumination of an optical microscope and analyzed in a dry state. All samples were previewed under the optical microscope in order to choose representative areas which could be compared systematically. In addition to these representative areas we found one cell in the experiment under high nutrient concentrations, incubated for 12 h in 5.8 mM $CaCl_2$ (9.3 times saturated), which was separated from the area of the droplet. Except for a small part, this cell appeared to be stripped out of its loosely bound EPS layer, which allowed us to investigate the interface between the cell and the $CaCO_3$-rich EPS layer which normally would require sectioning of the sample.

2.4. Sample preparation for the FIB milled sections

As only a fraction of cells mediate the precipitation of large crystals, conventional sample preparation methods

Table 1
Overview of the experimental conditions in the different $CaCO_3$ precipitation experiments.

$CaCl_2$ concentration	2.9 mM	5.8 mM
$NaHCO_3$ concentration	1.4 mM	1.4 mM
Calcite saturation Ω	6.0	9.3
Initial pH	8.29	8.26
	Sampling times techniques (nutrient conditions) (l, low; m, medium; h, high)	
Precipitation experiment with cells in exponential phase, sampling prior to the onset of calcite precipitation (cultured 25 days)	52 h STXM (l, h)	12 h STXM (l, m, h) TEM (h)
Precipitation experiment with cells in exponential phase, sampling after calcite precipitation (cultured 25 days)	144 h STXM (l, h)	n.a.
Precipitation experiment with cells in stationary/death phase (cultured 198 days)	52 h (STXM) (l)	n.a.

such as ultramicrotomy are not appropriate because the presence of a cell–mineral interface on a section is unlikely. Furthermore the embedding epoxy resins mask the C-1s spectral information about the biochemical composition of the sample. Therefore we prepared samples of cell–mineral interfaces by focused ion beam (FIB) milling which allowed for careful selection of the slice-plane. For this experiment it was essential to find early calcite precipitates which nucleated on cyanobacterial cells. The onset of precipitation coincides with the onset of a pH drop and a drop in electrical conductivity (Obst et al., 2005). Thus, we monitored the pH throughout the entire experiment in order to sample the cell suspension at the peak of calcite precipitation which started after 43 h in the 6.7 times saturated solution. Aliquots of the cell/mineral suspensions were sampled 71 h after the start of the incubation and were vacuum filtered using polycarbonate filters (Nucleopore, 0.2 μm pore size). After rapid air-drying the samples were sputter coated with platinum. After the selection of the slice plane, the area of interest was covered with a thin platinum layer by electron beam assisted deposition followed by a micron-thick layer of platinum by ion-beam assisted deposition. These platinum layers were essential in order to protect the sensitive organic material from the milling ion beam. Ultrathin sections of $CaCO_3$ crystals attached to cyanobacteria were then prepared by FIB milling using the lift out approach and optimizing the ion current and milling sequence in order to reduce the ion-beam induced damage to the sidewalls of the section (Obst et al., 2005). The ultrathin sections were deposited on carbon coated 200 mesh copper TEM grids using a micromanipulator.

2.5. STXM experiments

The samples were analyzed with the STXMs at the spectromicroscopy beamline 10ID-1 at the Canadian Light Source (CLS), Saskatoon, SK, Canada (Kaznatcheev et al., 2007), and STXM beamlines 5.3.2 (Kilcoyne et al., 2003) and 11.0.2 (Bluhm et al., 2006) at the Advanced Light Source (ALS), Berkeley, CA, USA. All beamlines were operated at an energy resolving power $E/\Delta E \geqslant 3000$. All samples were analyzed in 1/3 atmosphere of He. Whereas the energy scale of C-1s spectra could be calibrated by measuring CO_2 gas spectra before or after the measurements, the Ca-2p spectra were calibrated internally using the main $2p_{1/2} \rightarrow 3d$ resonance peak at 352.6 eV (Benzerara et al., 2004b).

Single-energy images at selected energies were recorded for navigation. Image difference maps were used for chemical mapping over relatively large areas. The recorded transmission images were converted to optical density (OD, absorbance) images, where $OD = -\ln(I \cdot I_0^{-1})$, I is the intensity at any pixel on the sample and I_0 is the incident intensity measured in an empty area adjacent to the sample. Semi-quantitative protein maps were derived from the difference of OD images recorded at 288.2 eV (peak of the C $1s \rightarrow \pi_{C=O}$ signal of protein) and 280 eV (prior to the onset of C-1s absorption signal) and for calcium from the OD image differences at 352.6 eV ($Ca_{2p1/2} \rightarrow Ca_{3d}$ resonance) and at 350.1 eV (in the dip between the $2p_{3/2}$ and $2p_{1/2}$ resonances). In order to obtain quantitative speciation maps, image sequences (stacks) were recorded with a spectral sampling of 100 meV at the C-1s (280–320 eV) and 80 meV at the Ca-2p (340–360 eV) edges in the spectral regions of interest. The spatial resolution of the image sequences was between 25 and 40 nm depending on the zone plate used and the pixel spacing. At the undulator beamlines (CLS 10ID1, ALS 11.0.2) all measurements were done with circular polarized light in order to avoid linear dichroism effects of the carbonate minerals (Metzler et al., 2007). After each image sequence an additional image was recorded at 289 eV in order to quantify X-ray beam-induced radiation damage to polysaccharides which are the most sensitive organic species in our samples (Dynes et al., 2006a). No significant radiation damage was observed during these measurements.

2.6. Reference compounds

In order to obtain NEXAFS reference spectra at the C-1s and Ca-2p edges, standard components were dry (minerals) or wet deposited onto Si_3N_4 windows. Human serum albumin was used as a reference compound for protein, xanthan gum was used as a reference for polysaccharides, and 1,2-dipalmitoyl-sn-glycero-3-phosphocholine as a lipid standard. All organic compounds were obtained commer-

cially (Sigma–Aldrich), except for human serum albumin, (Behringwerke AG), and the lipid, (Avanti Polar Lipids). Calcite, aragonite and vaterite were used as reference compounds for the calcium carbonates. The calcite (chips of a large single crystal) was kindly provided by Dr. H.P. Schwarz (School of Geography and Earth Sciences, McMaster University, Hamilton, ON, Canada). The aragonite (nacre of an abalone shell which then was purified in order to remove any organic content) was kindly provided by Dr. J. Rink (School of Geography and Earth Sciences, McMaster University, Hamilton, ON, Canada). The vaterite was synthesized according to the method of Kralj et al. (1994) and has previously been characterized by STXM (Benzerara et al., 2004b). All reference samples were ground into a fine powder and dispersed on Si_3N_4 windows. Particles chosen for detailed study were of a size to have a total optical density OD < 2 in the case of C-1s and <0.8 in the case of the Ca-2p spectra in order to avoid potential spectral distortions associated with absorption saturation when thicker regions are used. A Ca-species standard of Ca adsorbed to the negatively charged polymers were prepared by adding $CaCl_2$ (0.1 M) to a suspension of xanthan gum. The suspension was centrifuged, the supernatant decanted and the xanthan gum was washed with deionized water in order to remove all Ca^{2+} which was not adsorbed to the polymer. This washing step was repeated three times. Another reference standard was prepared by adding *S. leopoliensis* to a solution of $CaCl_2$ without the addition of any bicarbonates. This solution, which was highly undersaturated ($\Omega << 10^{-3}$) with respect to any carbonate phases, was sampled 10 minutes after the addition of the cells. Spectra of the Ca^{2+} adsorbed to the polymers were then extracted from image sequences at the Ca-2p edge. At the same time it was verified at the C-1s edge that the samples did not contain carbonate in order to make sure that the Ca^{2+}-spectra are representative for an adsorbed species. The results of both approaches were similar. For the quantitative mapping the spectrum obtained from the *S. leopoliensis* EPS was used. Furthermore a standard of dissolved $CaCl_2$ was measured (~50 mM) in a sandwich of two Si_3N_4 windows (i.e. wet cell) with a solution layer of ~1 μm. All spectra were normalized to an optical density appropriate for a 1 nm layer of the compound. Therefore the measured reference spectra were scaled to match the absorption in the pre- and post-edge regions predicted from the elemental composition, densities and tabulated atomic scattering factors (Henke et al., 1993). Model spectra were set to an absolute linear absorbance scale (OD per nm effective thickness) using aXis2000 (Hitchcock, 2008) and assuming the appropriate elemental ratios and densities for each individual compound (organic compounds, dissolved and adsorbed Ca^{2+} 1 g cm^{-3}, calcite 2.71 g cm^{-3}, aragonite 2.93 g cm^{-3}, vaterite 2.66 g cm^{-3}, (Barthelmy, 2000)).

2.7. Data analysis and speciation mapping

Images and image sequences from the cell preparations were analyzed using the aXis2000 software package (Hitchcock, 2008). The image sequences were aligned and converted to optical density scale OD. According to Lambert Beer's law the optical density is directly proportional to the amount of the individual compound in the X-ray beam path, which allowed us to derive quantitative maps of chemical species from our samples based on a linear combination of the normalized NEXAFS spectra of the individual compounds. Composition maps were obtained by singular value decomposition (SVD) (Koprinarov et al., 2002) of the C-1s image sequences which were fit with the reference spectra for protein, polysaccharides, lipids, carbonate and the spectrum of H_2O which has no spectral features at the C-1s edge. All reference spectra were on a linear absorbance scale (per nm) so the gray scales of each component map, which are constructed from the SVD fit coefficients, give the effective thickness (in nm) of that component at each pixel, assuming the density is the same as that in the reference compound. This approach has been described previously by Dynes et al. (2006a).

Because of the extremely sharp and intense Ca 2p-3d resonance peaks further data treatment was required at the Ca-2p edge. In order to avoid problems with absorption saturation (i.e. affects quantification by underestimating it), the images within 0.3 eV of the energies of the two highest resonance peaks (349.3 and 352.6 eV) were removed from the image sequence if the OD at the peak maximum was higher than 1. The image sequences were then decomposed into their principal components (Lerotic et al., 2004) using the principle component analysis algorithm written by C. Jacobsen (V1.1, 1999) which is included in aXis2000. Reference spectra of calcite, aragonite, vaterite, Ca^{2+} adsorbed to EPS and a calculated spectrum of organic carbon "CH_2O" which has no spectral features at the Ca-2p edge were used as target spectra and fitted with the principle components. The obtained fits were then used as for the SVD mapping as described earlier.

The precision (statistical fluctuation) of the SVD fitting procedure has previously been estimated to be in the range of few percent (Dynes et al., 2006b) and the accuracy is limited by systematic errors such as incorrect elemental compositions in the calibration of the reference spectra and a potentially incorrect selection of model compounds for the fit, which is rather unlikely as described later.

2.8. X-ray diffraction measurements

Samples for X-ray diffraction measurements were prepared in the same way as those for STXM measurements. As a last step, the Ca-incubated cell suspension was centrifuged and the supernatant was decanted carefully. The viscous wet cell paste was then deposited onto a quartz (Z/10 sample) or glass window (Z sample) which resulted in a ~0.5 mm thick layer of cells in an area of ~10 mm diameter. X-ray diffraction was measured with a Rigaku Rotaflex equipped with a 3.2 kW CuK_α source, located at the Geology Department of the University of Saskatchewan, Saskatoon. The angles were scanned from 20 to 60° at a speed of 2° min^{-1}. The dataset of the sample on the quartz window is presented as raw data whereas the broad glass band between the angles $2\theta = 20 - 30°$ was subtracted from the dataset of the sample on the glass slide.

2.9. Transmission electron microscopy (TEM)

In order to prevent sample preparation artifacts in determining the mineralogy, whole cells were used for the electron diffraction experiment (for the experimental conditions see Table 1). After incubation in the $CaCl_2$/$NaHCO_3$ solution, lacey carbon coated Cu TEM grids were dipped into the cell suspension. The resulting water droplet was removed from beneath with a filter paper. The grids were then rapidly dried and stored in a desiccator. As this procedure does not preserve the cell internal ultrastructure it was not used for structural investigations. However, the procedure was optimized in order to minimize sample preparation artifacts affecting the potentially sensitive layer of calcium carbonate within the EPS layer around the cells; other techniques such as chemical fixation of the cells or high pressure freezing followed by freeze substitution and embedding in a resin involve either aqueous solvents which could easily dissolve a thin amorphous $CaCO_3$ phase or organic solvents which could potentially affect the polysaccharide-rich EPS layer.

The electron micrographs and electron diffraction patterns were recorded with a Jeol 2010 (LaB_6) at 200 kV located at the Physics Department of the University of Alberta, Edmonton. The instrument was equipped with an AMT Hamamatsu CCD camera.

3. RESULTS

3.1. Identification of involved Ca-species

FIB-milled thin sections of cell–mineral interfaces were analyzed in order to identify all mineral phases involved in biomineralization of calcite by *S. leopoliensis*. The use of a dual-beam FIB for the preparation facilitated the selection of representative cells as the electron beam could be used for prescreening large sample areas without destroying the areas of interest. Ultrathin sections were prepared from *S. leopoliensis* cells with one or several small $CaCO_3$ crystals of different sizes attached (Fig. 1, lower image). These sections were analyzed by STXM. The extracted Ca-2p spectra were compared to the spectra of several Ca-containing reference compounds (Fig. 1, left) such as calcite, aragonite, vaterite, Ca-hydroxyapatite, dissolved Ca^{2+} (from $CaCl_2$ solutions), and Ca^{2+} adsorbed to extracellular polymers such as xanthan gum and the polymers produced by

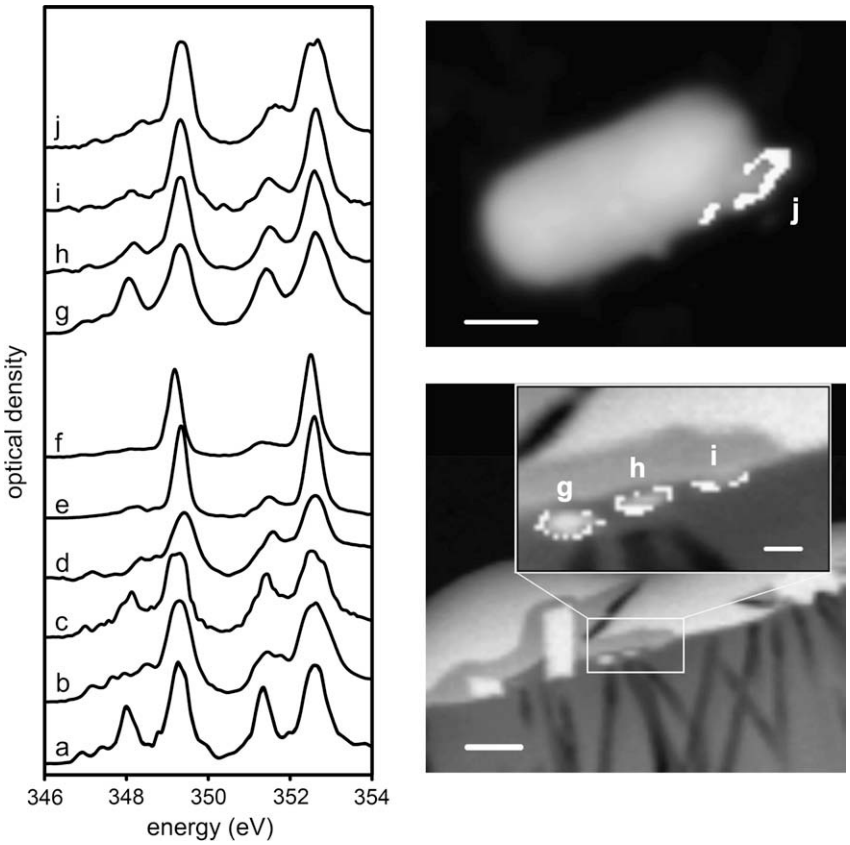

Fig. 1. (Lower right) STXM image of a focused ion beam milled ultrathin section (scale bar 1 μm); (inset) an enlarged section of this image (scale bar 200 nm). (Upper right) average of an image stack across the Ca-2p edge of a *Synechococcus* cell (scale bar 500 nm) with $CaCO_3$ attached (j). This cell was analyzed and presented in detail in Figs. 3 and 4. (Left) Ca-2p spectra of (a) calcite, (b) aragonite, (c) vaterite, (d) Ca-hydroxyapatite, (e) dissolved Ca^{2+} from $CaCl_2$ and (f) Ca^{2+} adsorbed to EPS. Spectra extracted from an image sequence at the locations indicated by the letters on the insert of the enlarged section of the lower image and the upper image. The spectrum of the large crystal (g) matches that of calcite, whereas the spectrum of the medium crystal (h) is similar to that of aragonite, overlaid by the spectrum of Ca^{2+} adsorbed to EPS. The spectrum of a non-crystalline hot spot of Ca (i) was similar to the spectra extracted from Ca^{2+} adsorbed to EPS.

S. leopoliensis (for the energies of the resonance peak positions see Table 2). The larger particle (Fig. 1g, diameter >300 nm) clearly showed the spectral signature of calcite with its characteristic 4-peak structure (348.0, 349.3, 351.3 and 352.6 eV), the smaller $CaCO_3$ rich particle in the center of the enlarged section (Fig. 1h) showed a composite of an aragonite-like spectrum with the two major peaks at 349.3 and 352.6 eV and a spectrum of Ca adsorbed to the EPS of *S. leopoliensis* (see spectra b and f in Fig. 1). Another hot spot of Ca (Fig. 1i), which did not show the specific $1s \rightarrow \pi_{C=O}$ carbonate resonance peak at 290.3 eV, showed Ca-2p spectra similar to those measured from Ca^{2+} adsorbed onto EPS produced by *S. leopoliensis* and xanthan gum. Analyzing NEXAFS spectra of FIB-milled thin sections, it has to be considered that a thin layer (few to several tens of nm) at each sidewall of the section is potentially affected by the ion beam, which could result in a partial amorphization of a mineral sample (Lee et al., 2007). The thickness of the affected layer can be reduced by optimizing the FIB-milling procedure (Obst et al., 2005).

The spectral signatures of aragonite (b) with the characteristic split peak at 351.4 eV and a series of small pre-edge peaks were found and extracted from samples of intact cyanobacterial cells (Fig. 1j). Based on the similar short-range order as determined from NEXAFS spectroscopy from here on we refer to this biogenic $CaCO_3$-phase precipitated by the cyanobacteria as aragonite-like $CaCO_3$.

Initially combinations of calcite, aragonite, Ca^{2+} adsorbed and vaterite spectra were included in the SVD mapping procedure. However, when vaterite was used it resulted in negative fits in all cases, which indicates that the composition model was over-parameterized. Vaterite and aragonite spectra were then individually removed from the composition model which resulted in lower standard deviations of the fits when aragonite was included and vaterite excluded compared to the case when vaterite was included and aragonite excluded. This led us to conclude that the analyzed samples did not contain significant amounts of vaterite-like $CaCO_3$. Therefore the vaterite spectrum was not included for the final quantitative mapping. All samples investigated contained spectral signatures of aragonite and Ca^{2+} adsorbed to EPS. As expected from the experimental setup, calcite was only found in the FIB-prepared samples which were taken after extended incubation times (e.g. 71 h in the example presented in Fig. 1). Calcite was included in the final SVD analysis where applicable, i.e. when significant fractions of calcite signal were found in the sample, and it was removed from the final fit when calcite was not found in order to avoid negative fits of an insignificant component with an over-parameterized model.

3.2. Characterization of the whole-cell samples

The sample preparation procedure of wet deposition followed by complete removal of the solution resulted in a relatively homogeneous distribution of *S. leopoliensis* PCC 7942 cells on the surface of the Si_3N_4 membranes (e.g. Fig. 2a) in the area where the droplet was left at the time the solution was removed. Protein- (Fig. 2b) and Ca-maps (Fig. 2c) of relatively large areas were then obtained by STXM in order to identify representative single cyanobacteria for detailed analysis (e.g. as indicated by the boxes in Fig. 2b and c).

In order to investigate the very first stages of $CaCO_3$ precipitation, samples for whole-cell experiments were taken close to the calculated induction time for calcite nucleation and deposited on Si_3N_4 windows. Single planktonic cells were analyzed at both the C-1s and Ca-2p edges. In order to biochemically characterize the $CaCO_3$ nucleation sites, carbon maps of the most abundant organic components were derived from the C-1s image sequences (see for example Fig. 3a). The central part of the cell is mainly composed of protein, but also contains polysaccharides and lipids. The strong background absorption is caused by hydration water and inorganic components of the cell. The cell is surrounded by a layer of strongly bound EPS which contains mainly polysaccharides followed by lipids and a small amount of proteins.

The carbon species maps were compared and correlated to the Ca-speciation maps (see Fig. 3b). Unlike all other cells which had been chosen to be representative, the cell displayed in Fig. 3a and b was found far outside the area where the droplet was left after the water was removed from the Si_3N_4 window during sample preparation. The cell shown here was exposed to shear stress and the loosely bound EPS was stripped off except for the lower right area where an ~200 nm thick piece of the $CaCO_3$-rich, weakly bound EPS layer remained at the surface. This cell showed particularly well the association of the aragonite-like $CaCO_3$ layer with the polysaccharide-rich polymer (compare polysaccharide map and map of aragonite-like $CaCO_3$ in Fig. 3a with the Ca-species maps of aragonite-like $CaCO_3$ and adsorbed Ca^{2+} in Fig. 3b), and a lipid- and polysaccharide-rich compound mainly at the interface between the aragonite-like $CaCO_3$ and the cell itself. The spa-

Table 2
Energies (eV) of the peak centers of Ca-2p signals from selected Ca-species (±0.1 eV).

Calcite	Aragonite	Vaterite	Ca-hydroxyapatite	Dissolved Ca^{2+}	Adsorbed Ca^{2+}
346.9	347.2	347	347.2	347	
347.4	347.7	347.3	347.7	347.6	
348	348	348.1	348.4	348.1	348.2
	348.5	348.6	348.7		348.7
349.3	349.3	349.2	349.4	349.2	349.3
351.3	351.4	351.4	351.6	351.4	351.5
352.6	352.6	352.6	352.6	352.6	352.6

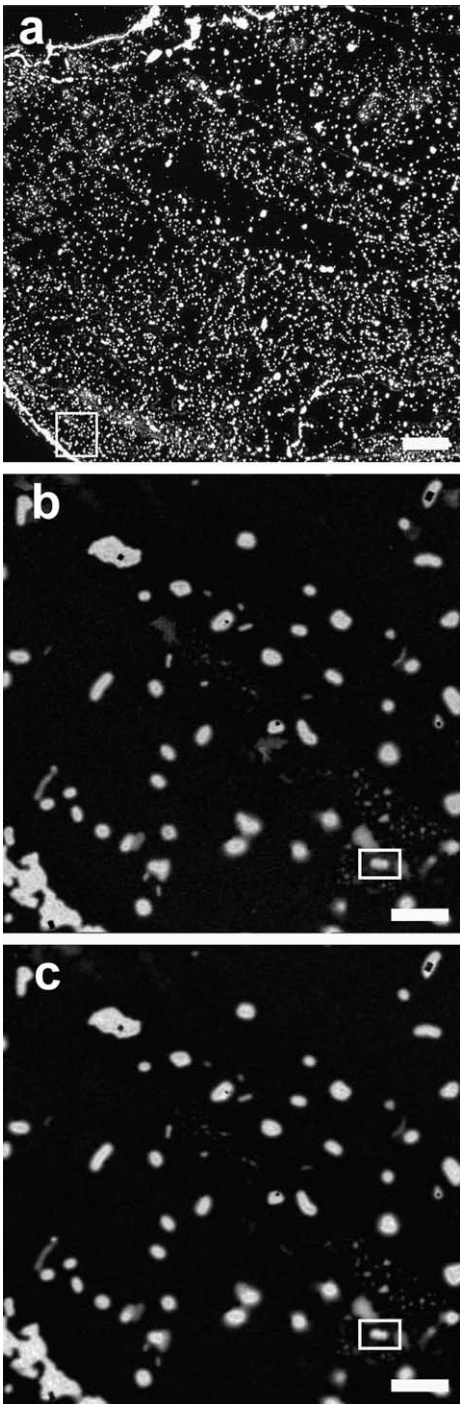

Fig. 2. Overview of a typical STXM sample. (a) Visual darkfield-image of the whole Si_3N_4-window with attached cyanobacteria (scale bar 100 μm). The box in (a) indicates the position of the protein map (b) and the Ca-map (c) which were obtained from STXM image differences at specific energies (scale bars 10 μm). The boxes in (b) and (c) indicate the cell which was analyzed in detail by acquiring image-stacks at the C-1s (Fig. 3a) and Ca-2p edges (Fig. 3b).

tial arrangement and the dimensions of the extracellular polymers however might be affected by the sample preparation.

3.3. Influence of nutrient conditions on $CaCO_3$ nucleation

Fig. 4 shows a systematic comparison of color composite component maps of Ca-species (spectroscopically identified as aragonite-like $CaCO_3$ (green) and adsorbed Ca^{2+} (blue)) for cells grown under low ($Z/10$), medium ($Z/4$) and high (Z) nutrient concentrations and incubated under a Ca-concentration of 5.8 mM for 12 h. The right hand panels of Fig. 4 display species profiles across the cells averaged over the areas indicated by the dotted lines in the color maps. Ca^{2+} is adsorbed onto EPS in similar amounts for all three treatments, with a slightly decreasing tendency (92 ± 6, 85 ± 5 and 68 ± 7 nm at the cell center ± 150 nm for cells cultured in $Z/10$, $Z/4$, Z media, respectively), whereas the amount of the aragonite-like $CaCO_3$ increases with increasing nutrient concentration (46 ± 6, 86 ± 9 and 140 ± 5 nm at the cell center ± 150 nm). Furthermore both the adsorbed Ca^{2+} and the aragonite-like $CaCO_3$ extend further from the cell in the case of high nutrient concentrations. This was most obvious in the projected average profiles of the Ca-species as a function of distance from the projected cell center. Quite noticeable in the projection profiles in Fig. 4 is a rim of the aragonite-like $CaCO_3$ around the cells which was most pronounced in the experiment with cells cultured under high nutrient concentrations.

Although Ca-2p NEXAFS spectroscopy clearly indicated the presence of a $CaCO_3$ phase with aragonite-like short-range order, it was not possible to recognize this layer morphologically or to detect nano-crystals within the EPS layer by scanning electron microscopy (SEM) or scanning transmission electron microscopy (data not shown). The presence of the aragonite-like $CaCO_3$ was however confirmed independently (e.g. Fig. 3a) by analyzing the near edge fine structure of C-1s edges, which showed the characteristic peak of the carbonate $1s \rightarrow \pi_{C=O}$ transition at 290.3 eV (Benzerara et al., 2004b). Since absorbance (OD) is linearly correlated with amount, the speciation maps derived from the C-1s and the Ca-2p edges are quantitative and thus the projection profiles give effective thickness of each component in nm. The amounts of $CaCO_3$ derived from the C-1s and the Ca-2p edges were similar; any deviations in amounts in any region were normally $<50\%$, with larger deviations in thick areas where the carbonate peak in the C-1s spectra might be saturated. In most areas the deviation was $<25\%$.

Although less visible, careful inspection of the Ca-2p speciation maps revealed small, needle-like structures in the aragonite maps for the experiment with cells cultured under low nutrient conditions ($\Omega = 9$, Table 1). In order to make these structures more visible, an image was taken right at the resonance peak of the $Ca_{2p\text{-}L3}$ transition at 352.6 eV (Fig. 5). According to the Ca-2p component maps (Fig. 4a), these needles consisted mostly of aragonite-like $CaCO_3$, associated with some adsorbed Ca^{2+}. These needles were closely associated with, but extended from the aragonite-like rim which was bound to the cell surface. The effective thicknesses of the needles of aragonite-like $CaCO_3$ derived from the Ca-2p map was similar ($\pm 30\%$) to the effective thicknesses derived from the C-1s maps (not shown). The effective thickness measurements were also

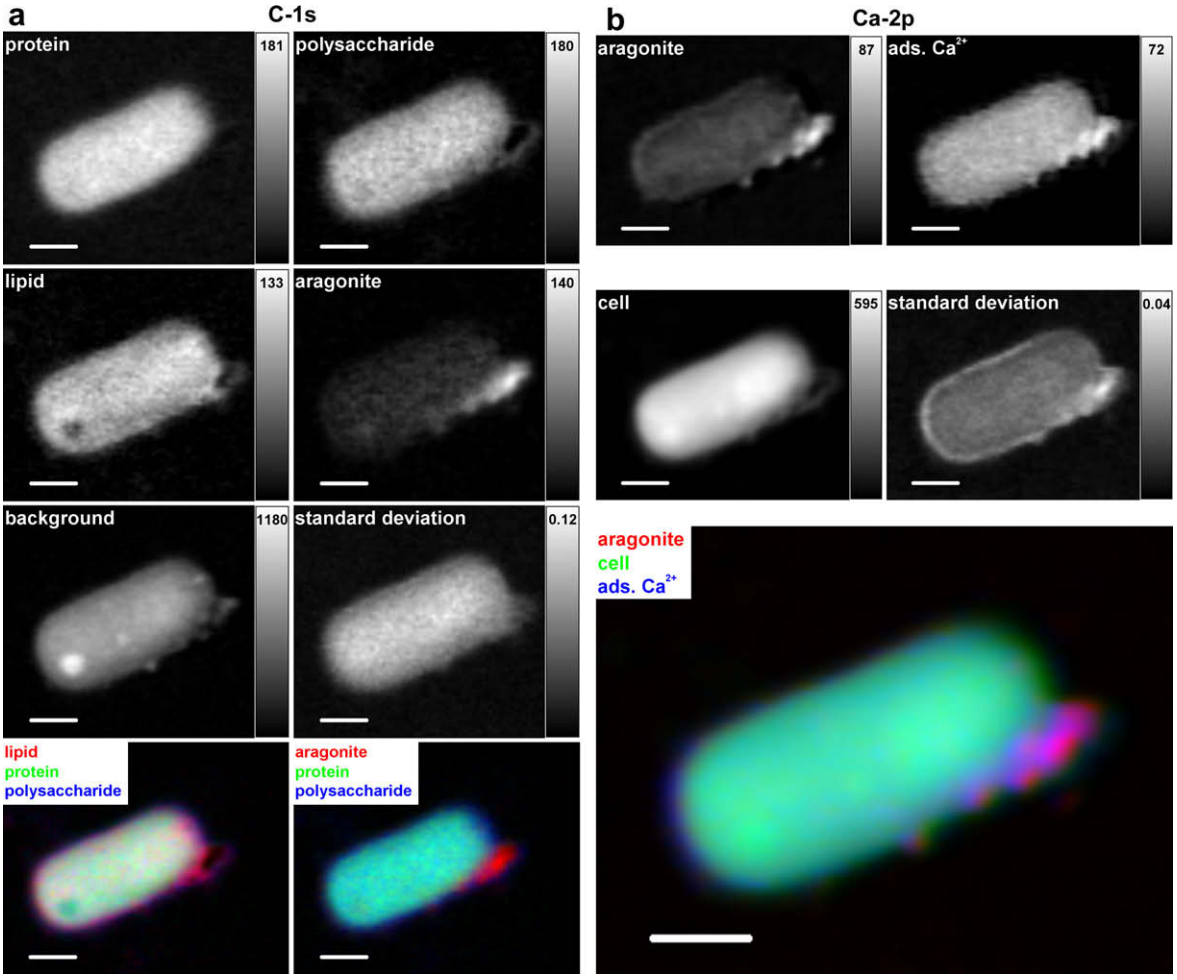

Fig. 3. (a) Carbon speciation maps of a *S. leopoliensis* PCC 7942 cell derived from singular value decomposition of a STXM image sequence at the C-1s edge using spectra of pure reference compounds (scale bars 500 nm). All gray scale maps are quantitative and presented on a effective thickness gray scale in nm. Each map shows the sum amount of the individual species as a function of the position and represents a 2D projections of the 3D objects. The protein map represents the cyanobacterial cell, which is surrounded by an EPS layer that is dominated by large amounts of polysaccharides and smaller amounts of lipids. Parts of the EPS of this cell were ripped off due to shear stress during sample preparation, so that only the more strongly bound fraction of the EPS embedds the cell homogeneously. Only at a small fraction of the cell, the loosely bound EPS (polysaccharides and lipids) and the embedded part of the aragonite-like $CaCO_3$ layer remained on the cell surface (lower right corner). The background-map is fitted by a spectrum that does not show any spectral features at the C-1s edge and therefore represents all elements absorbing in the pre-edge of C-1s. The color overlays are presented with individually rescaled red, green and blue channels in order to show the spatial correlation of the individual components. (b) Calcium speciation maps of a *S. leopoliensis* PCC 7942 cell derived from singular value decomposition of a STXM image sequence at the Ca-2p edge using spectra of pure reference compounds (scale bars 500 nm). Parts of the EPS and the Ca^{2+} adsorbed to this fraction of the polymer were ripped off due to shear stress during sample preparation. At one spot the loosely bound EPS and the embedded aragonite-like $CaCO_3$ layer remained on the cell surface. This facilitated the extraction of the spectra of the individual species since the compounds were spatially separated. The cell-map represents all elements absorbing in the pre-edge of Ca-2p, which in this case is mainly carbon. All gray scale maps are quantitative and presented on effective thickness scale in nm. The red, green and blue channels of the color overlay are rescaled individually.

consistent with the lateral dimensions of the needles, which were in the range of 40–100 nm (Fig. 5), a dimension which includes both the aragonite-like $CaCO_3$ and the adsorbed Ca-species. Considering the pixel size of 40×40 nm^2 in this experiment and the spot size of the X-ray beam (30 nm) the absorption of objects smaller than the actual spot size can be slightly underestimated. Thus, we expect the real thickness of the needles of aragonite-like $CaCO_3$ to be in the range of 20–50 nm, associated with an equal amount of the adsorbed Ca^{2+} species in the EPS. Similar structures were not observed at other sampling times or different sample treatments.

After 52 h of incubation under a Ca-concentration of 2.9 mM, cells were surrounded by lower amounts of both Ca^{2+} adsorbed to EPS and aragonite-like $CaCO_3$ (Fig. 6a–d). Whereas the amount of Ca^{2+} adsorbed to EPS increased only slightly with increasing nutrient concentration (31 ± 4, Fig. 6a, and 52 ± 6 nm, Fig. 6c, for cells

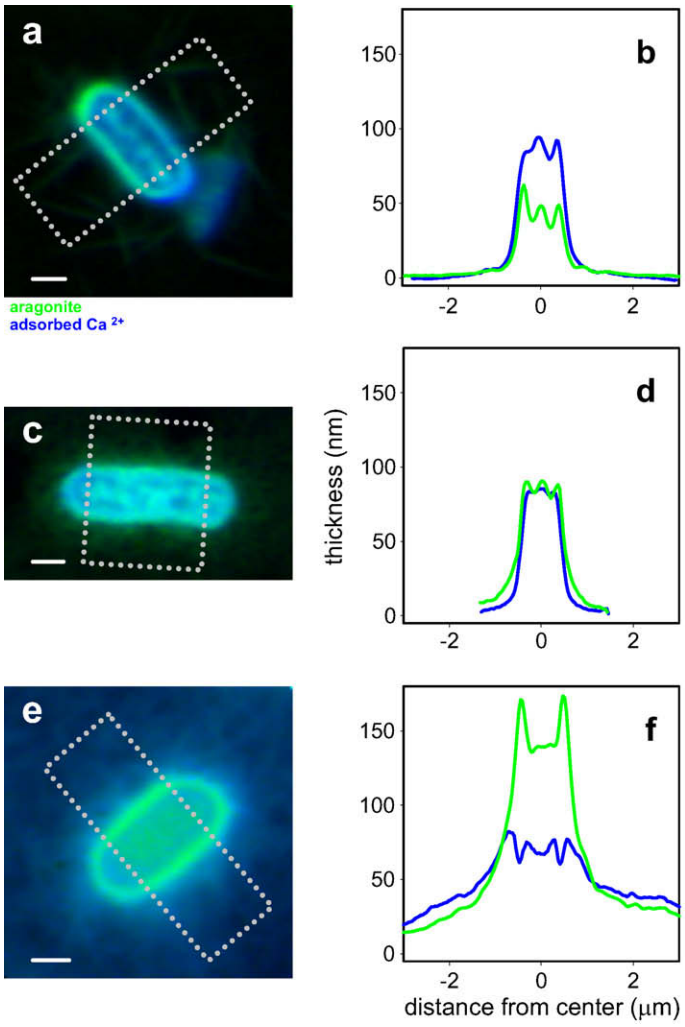

Fig. 4. (Left) Ca-speciation maps of aragonite-like $CaCO_3$ (green) and Ca^{2+} adsorbed to EPS (blue) of cells grown under low (a), medium (c), and high nutrient concentrations (e). All cells were incubated for 12 h in 5.8 mM Ca^{2+}. (Scale bars 500 nm) (Right) Intensity profiles (b, d and f) extracted from the areas marked with dotted lines and present average projection profiles across the individual cells.

cultured in $Z/10$ and Z media, respectively), the amount of aragonite-like $CaCO_3$ increased significantly from 17 ± 3 to 77 ± 8 nm at the cell center ± 150 nm). The Ca-rich rim around the cell in the projection image was dominated by adsorbed Ca^{2+} in contrast to the experiment at a Ca-concentration of 5.8 mM where the rim was observed in the maps of aragonite-like $CaCO_3$. In the experiment with a Ca^{2+} concentrations of 2.9 mM the distribution of aragonite-like $CaCO_3$ was inhomogeneous and patchy in the case of the low-nutrient cultures (Fig. 6a) whereas it was more homogeneous in the case of the high nutrient cultures (Fig. 6c). In both cases the aragonite-like $CaCO_3$ seemed to originate very close to the cell surface.

The same experiment was repeated after 144 h of incubation in the $NaHCO_3/CaCl_2$-solution (Fig. 6e–h). Compared to the 52 h incubation, the amount of Ca^{2+} adsorbed to the EPS was significantly reduced for cells cultured under both low and high nutrient concentrations (13 ± 2 and 7 ± 1 nm at the cell center ± 150 nm). The distribution of the adsorbed Ca^{2+} species was inhomogeneous in both cases. Moreover, aragonite-like $CaCO_3$ was absent in cultures at low and high nutrient concentrations in the 144 h incubations (both <1 nm at the cell center).

Whereas all the results described so far were obtained from cells harvested at the exponential growth phase, the results presented in Fig. 6i–o were obtained from cells cultured in low nutrient culture medium ($Z/10$) for an extended period of 198 days, which represents the end of the stationary growth phase and beginning of the death phase. The adsorption of Ca^{2+} and the nucleation of aragonite-like $CaCO_3$ were heterogeneous at the single cell and at the intercellular level. The amounts of Ca^{2+}adsorbed to EPS was smaller on average (5 ± 1, 6 ± 1, 14 ± 5, 24 ± 2, 23 ± 1, 19 ± 2 and 30 ± 2 nm at the cell center ± 150 nm) compared to the experiment with cells in the exponential phase (30 ± 5 nm at cell center). The amounts of aragonite-like $CaCO_3$ (1.2 ± 0.6, 1.2 ± 0.6, 6 ± 3, 1 ± 1, 0.8 ± 0.8, 1.6 ± 1, 4 ± 2 at the cell center ± 150 nm) were

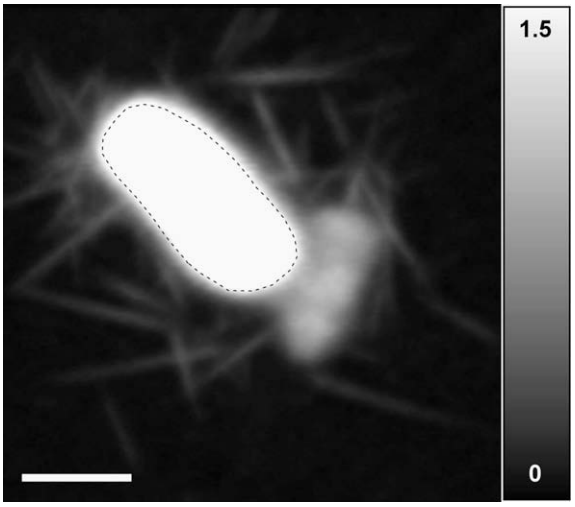

Fig. 5. Ca-2p image of a cyanobacterial cell surrounded by needle-like structures. This image was acquired at the Ca L_2 resonance peak at 352.6 eV and converted to OD. In order to enhance the visibility of the needle-like structures, the grayscale was limited to 1.5 OD units which saturates the display in the central part of the image marked by the dashed line (scale bar 1 μm).

significantly smaller compared to the experiment with cells in the exponential growth phase (17 ± 3 nm at the cell center ± 150 nm).

3.4. Crystallinity of the precipitates

No peak was observed by XRD measurements on samples of cyanobacteria cultured under low ($Z/10$) nor high (Z) nutrient concentrations, indicating that the samples were amorphous in bulk X-ray diffraction (see Electronic annex EA-1). When the sample was analyzed using selected area electron diffraction in a TEM (see EA-2), some areas of the cell exhibited a very weak diffraction pattern which indicated well-crystallized grains. However the $CaCO_3$ layer with aragonite-like short-range order showed only a broad ring structure characteristic for an amorphous or poorly crystallized $CaCO_3$.

4. DISCUSSION

4.1. Suitability of STXM for the characterization of cyanobacterial calcification

STXM combines the chemical speciation sensitivity of NEXAFS spectroscopy with high spatial resolution and has been shown to be capable of mapping the biochemical composition of bacteria and biofilms at a subcellular scale (Benzerara et al., 2006, 2004b; Bluhm et al., 2006; Dynes et al., 2006a,b). It has been demonstrated that the near edge fine structure of the Ca-2p absorption-edge is strongly dependent on first shell coordination and the detailed structure surrounding the Ca^{2+} ion, in particular the crystal field (de Groot et al., 1990; Himpsel et al., 1991; Naftel et al., 2001; for a review see de Groot, 2005). The Ca-2p edge has been used recently to characterize Ca-containing mineral phases like the three most common polymorphs of $CaCO_3$, vaterite (O coordination number 6), aragonite (O coordination number 9) and calcite (O coordination number 6) (Doyle et al., 2004). A more detailed spectro-microscopical characterization of Ca-containing minerals by STXM has shown that they are unambiguously identified by their Ca-2p spectra (Benzerara et al., 2004b).

Weiner et al. (2003) recommended the combination of Raman and EXAFS spectroscopy for investigations of amorphous $CaCO_3$ precursor phases. The chemical sensitivity of this combination is excellent and EXAFS provides information on the short-range order within the amorphous mineral phase. However, due to a relatively poor spatial resolution, this combination is not capable of investigating cyanobacterial $CaCO_3$ biomineralization of individual cells for which a spatial resolution in the sub 100 nm range is essential. Gradients and chemical microenvironments around planktonic cells are also very difficult to investigate with more conventional techniques such as confocal laser scanning microscopy (CLSM) because its resolution is at best ~250 nm lateral and ~700 nm vertical (Neu and Lawrence, 2005). TEM offers the required spatial resolution for this investigation, but has limited speciation capabilities and standard sample preparation steps produce artifacts leading for example to an underestimation of EPS surrounding the bacteria (Hunter et al., 2008). Moreover, uranyl-acetate and lead-citrate solutions, which are the most common stains used for contrasting ultrathin sections of biological samples, rapidly dissolve $CaCO_3$ precipitates tens of nm in size.

Thus, STXM is ideally suited for investigating (i) the organochemical composition of the nucleation sites of the biogenic $CaCO_3$ precipitates and (ii) both the adsorbed and carbonate Ca-species involved in the early stages of calcite precipitation by *S. leopoliensis* PCC 7942 and in particular to analyze the involvement of potential precursor phases in the nucleation process. In particular spectromicroscopy using STXM has the advantage of a very high spatial resolution (currently ~25 nm) which is the same spatial scale as critical mineral nuclei which are typically in the range of 1–100 nm (De Yoreo and Vekilov, 2003). STXM furthermore has the advantage of reduced radiation damage compared to TEM electron energy loss spectroscopy (Hitchcock et al., 2008).

4.2. Characterization of the $CaCO_3$ with respect to its structure

Each of the spectromicroscopic datasets consisted of several thousands of NEXAFS spectra (one per pixel of the analyzed area). These spectra represent the sum of the spectral contributions of all the individual chemical species that are present at this spot of the sample. The speciation maps (Figs. 3, 4 and 6) were the result of the quantitative statistical analysis of these datasets.

NEXAFS spectra that were extracted of the $CaCO_3$ layer closely attached to the cell surface (see Figs. 1j, 3b and 4) and associated with a dense layer of polysaccharide-rich polymer embedding the cells was very similar to that of aragonite (Fig. 1b) and could clearly be differenti-

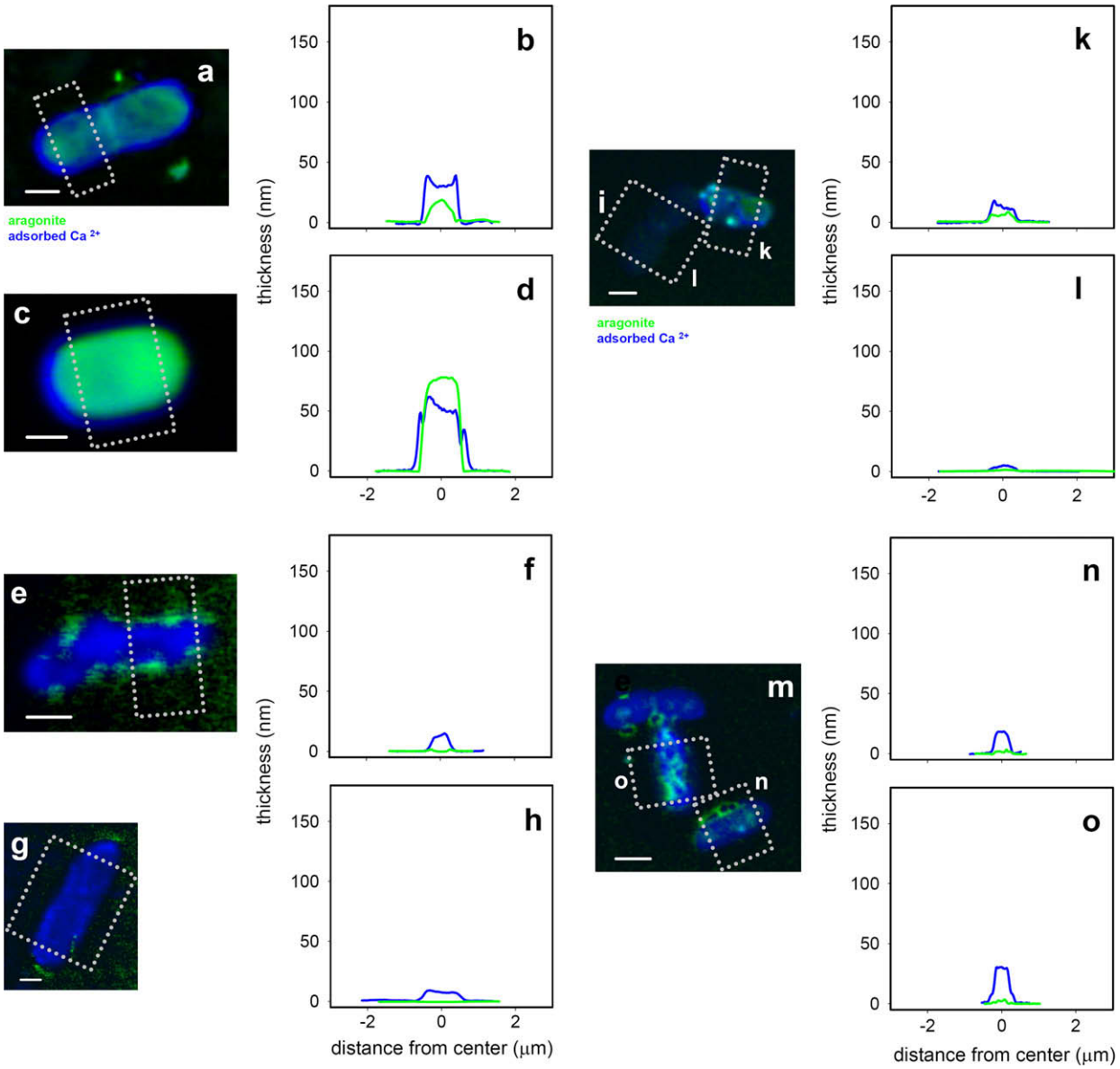

Fig. 6. (Left) Ca-speciation maps of aragonite-like $CaCO_3$ (green) and Ca^{2+} adsorbed to EPS (blue) of cells grown under low (a and e), high nutrient concentrations (c and g). After cultivation the cells were incubated for 52 h (a and c) and 144 h (e and g) in 2.9 mM Ca^{2+}. The 52 h represented the induction time for calcite nucleation, whereas the 144 h represented a time period wherein calcite precipitation was advanced. Intensity profiles (b, d, f and h) were extracted from the areas marked with dotted lines and present average projection profiles across the individual cells. (Right: i, m) Two examples of Ca-speciation maps of aragonite-like $CaCO_3$ (green) and Ca^{2+} adsorbed to EPS (blue) of cells grown under low nutrient concentrations and harvested at the end of the constant phase (198 days). After cultivation for 198 days, the cells were incubated for 52 h in 2.9 mM Ca^{2+}. Intensity profiles (k, l, n and o) were extracted from the areas marked with dotted lines and present average projection profiles across the individual cells. (all scale bars 500 nm).

ated from all other Ca-species such as aqueous Ca^{2+} (Fig. 1e), Ca^{2+} adsorbed to EPS (Fig. 1f), and from crystalline phases of vaterite (Fig. 1c), calcite (Fig. 1a) and Ca-hydroxyapatite (Fig. 1d). Based on its spectroscopic signature the short-range order of the $CaCO_3$-layer was therefore identified to be aragonite-like.

We observed the nucleation of this aragonite-like $CaCO_3$ layer on all of our samples where there were viable cells prior to the onset of calcite precipitation. In contrast to this very homogeneous nucleation of the aragonite-like $CaCO_3$ polymorph, calcite precipitated on a fraction of the cyanobacteria only. The Ca-2p NEXAFS fingerprint of four FIB-milled ultra-thin sections of $CaCO_3$ crystals >300 nm precipitated by *S. leopoliensis* PCC 7942 cyanobacteria indicated that these crystals were solely composed of calcite (Fig. 1g and a). All crystals larger than ~300 nm had the calcite signature and no significant amounts of other mineral phases were observed for crystals of this size

range. This is consistent with observations of previous studies of the same strain wherein crystals were analyzed by electron microscopy (Obst et al., 2005) and a number of environmental studies where *Synechococcus* strains were observed to be responsible for larger scale calcite precipitation, so-called whiting events (Thompson et al., 1997).

The $CaCO_3$ around the cells (Fig. 1j) and the smaller areas containing $CaCO_3$ in the FIB sections (Fig. 1h) of this study had the spectral fingerprint of aragonite (Fig. 1b). The latter is likely to be a tangential section of a *Synechococcus* cell. Another particle on the same sample which was previously mapped as a hot spot of Ca did not show the typical carbonate peak at 290.3 eV. The spectral signature at the Ca-2p edge was very similar to those obtained from Ca^{2+} adsorbed to polysaccharides. The presence of these three Ca-species in the same sample coincides with the fact that this sample was collected close to the induction time when precipitation of calcite is starting.

Our study indicates that either the aragonite-like $CaCO_3$ layer or the interface between the negatively charged polymers and the solution outside the carbonate layer might act as the template for calcite nucleation. Further investigations of cell–mineral interfaces are necessary in order to identify where exactly the calcite nuclei originate with respect to the aragonite-like $CaCO_3$ rich layer. However, it is clear that the aragonite-like $CaCO_3$-layer is a transient precursor phase of the subsequent calcite precipitation. Thus, the precipitation of calcite which results in large crystals (microns and tens of microns size) seemed unlikely to be controlled by *S. leopoliensis* (Obst et al., in press).

Under our experimental conditions, the aragonite polymorph is thermodynamically less favorable and the supersaturation with respect to aragonite significantly lower compared to calcite (Plummer and Busenberg, 1982). In principle calcite precipitation can be kinetically inhibited, e.g. by the presence of phosphates (Dove and Hochella, 1993; Hartley et al., 1995; Rodriguez-Navarro et al., 2003), by Mg^{2+} which is a major inhibitor of calcite precipitation in seawater (Zuddas and Mucci, 1994; Zhang and Dawe, 2000), or by organic compounds (Lebron and Suarez, 1998; Zuddas et al., 2003; Bosak and Newman, 2005). Since neither phosphates nor Mg^{2+} were present in the precipitation experiments of this STXM study, the occurrence of a precursor phase with aragonite-like short-range order suggests a strong influence of organic compounds, specifically the composition, structure and concentration of the bacterial EPS on mineral nucleation and precipitation.

Similar to the results of this study, bacterial control of crystal structure could also explain the observations of Lopez-Garcia et al. (2005) who observed aragonite nano-crystals in the size range of a few tens of nm closely associated with bacteria in a study of $CaCO_3$ microbialites precipitated in a hypersaline lake; these authors also observed inorganically precipitated calcite. Furthermore, our results are in keeping with those of Braissant et al. (2003) who observed that purified EPS influenced the crystal structure and morphology in a study of $CaCO_3$ precipitation in terrestrial environments. Particularly at high concentrations of xanthan EPS the authors measured a preferential precipitation of vaterite compared to calcite in the presence of several L-amino acids. A strong influence on $CaCO_3$ precipitation by interactions of EPS with Ca^{2+}-ions has also been suggested for sulfate-reducing bacteria which have been shown to produce large amounts of EPS (Braissant et al., 2007).

Thus, the results of the present study clearly indicate that the extracellular polymers of *S. leopoliensis* PCC 7942 favor an aragonite-like short-range coordination of the precipitated phase and accelerate the nucleation and precipitation kinetics compared to the subsequent precipitation of the thermodynamically stable calcite.

4.3. Characterization of the aragonite-like $CaCO_3$ layer with respect to its crystallinity

The aragonite-like $CaCO_3$ layer precipitated on the surface of the *S. leopoliensis* PCC 7942 was rather thin and homogeneous. As explained in more detail in the following section, based on X-ray (EA-1) and electron diffraction data (EA-2), the aragonite-like $CaCO_3$ could be either truly amorphous or nano-crystalline; in either case it would fall into the category "amorphous calcium carbonate" based on the definition of this term by Addadi et al. (2003): ACC are $CaCO_3$ polymorphs which are isotropic in polarized light and do not diffract X-rays. However, Addadi et al. (2003) already stated that this term might not be specific enough as it has been shown that short-range order can exist in the coordination environment of ACC and it can be similar to crystalline forms like calcite or aragonite (Becker et al., 2003; Weiner et al., 2003; Lam et al., 2007).

Aragonite-like $CaCO_3$ with a crystal-like habit was only observed in the experiment with cells cultured under low nutrient conditions. Whereas the vast majority of the aragonite-like $CaCO_3$ was located within the EPS layer surrounding the bacteria and followed the shape of the bacterial surface, small needle-like structures extruded from this layer (Fig. 5). Based on the quantitative maps, the effective thicknesses of both aragonite-like $CaCO_3$ and the adsorbed Ca^{2+}-species (Fig. 4a) were determined to be 5–20 nm for each species with a small majority on the side of aragonite-like $CaCO_3$ for the same area.

No crystallized phase was observed by TEM or XRD in the experiments with cells grown under medium and high nutrient concentrations (e.g. Fig. 4c–f), where cells produced larger amounts of EPS (Obst and Dittrich, 2005) or under lower supersaturation (e.g. Fig. 6a–d). Furthermore the precipitated amount of aragonite-like $CaCO_3$ within the EPS increased with increasing nutrient concentration (Fig. 4) and decreased with lower supersaturation (Fig. 6a–d). Also it is noticeable that the aragonite-like $CaCO_3$ is concentrated in a small envelope around the cell surface which, in projection, results in a halo around the cell. This can be observed particularly well in Fig. 4a and e and the corresponding cross-sections (Fig. 4b and f). The halo indicates that the aragonite-like $CaCO_3$ is at a higher concentration in closely bound EPS (capsular-like), whereas the adsorbed species is found on both the closely bound and the weakly bound EPS which spreads out from the cell surface. In contrast to the strong influence of the nutrient concentration on the nucleation of aragonite-like

$CaCO_3$, cells grown under low nutrient concentrations adsorb similar amounts of Ca^{2+} as cells grown under medium nutrient concentrations, and both adsorb only slightly more than cells grown under high nutrient concentrations. Therefore, the difference in the amount of precipitation of aragonite-like $CaCO_3$ can not be explained simply by a difference in charge density resulting in lower concentrations of Ca^{2+} within the EPS. In combination, these results suggest that the amount, organochemical composition and structure of the closely bound EPS strongly influence or even control the stabilization of the aragonite-like $CaCO_3$.

In a bulk X-ray diffraction experiment with a conventional CuK_α X-ray source this cyanobacterially precipitated $CaCO_3$ did not show any significant diffraction peaks (see EA-1). This is in contrast but not in contradiction to the results of Rodriguez-Blanco et al. (2008) who recorded XRD patterns of abiotically precipitated amorphous calcium carbonate (ACC) and observed broad, diffuse maxima with a height of about five times the background noise level. This could mean that the biogenically precipitated, aragonite-like $CaCO_3$ in this study has less intermediate and long-range order compared to the abiotically precipitated phase in their study. However, it has to be considered that X-ray diffraction without spatial resolution is not particularly sensitive and rather large amounts of material are required to obtain detectable diffraction signals. Some researchers even claimed that a minimum crystal size in the order of tens of nanometers is required to detect a diffraction pattern using this technique (Lowenstam and Weiner, 1989). Selected area electron diffraction using TEM is more sensitive, particularly when dealing with small amounts of material and small crystals. When single cyanobacteria cells were analyzed in the TEM (EA-2), most of the cell area showed rather weak and very broad ring-like structures in diffraction mode, which is characteristic of amorphous material. This is in agreement with the results of Rodriguez-Blanco et al. (2008) who observed similar ring structures in the TEM-SAED analysis of single ACC globules (diameter 100–200 nm) which were precipitated abiotically from solution. When they exposed these globules to the electron beam for several minutes, they could induce crystallization and the formation of a more ordered structure. According to their interpretation this was caused by the loss of hydration water of the ACC. Similar effects were observed by (Politi et al., 2007) when they exposed the ACC to an electron beam. In contrast, in our study formation of a more ordered structure was not observed. A potential explanation for the difference could be that in our study the formation of long-range order could have been suppressed by the EPS matrix wherein the amorphous, aragonite-like $CaCO_3$ precipitated.

The nucleation of the amorphous aragonite-like $CaCO_3$ was found to be much more homogeneous and widespread compared to the subsequent nucleation of calcite (Obst et al., 2005, 2006): amorphous aragonite-like $CaCO_3$ was found on every cell which indicates that *S. leopoliensis* PCC 7942 mediated the precipitation, whereas calcite was found only on a small fraction of cells and usually appeared in μm-sized crystals. The latter result was consistent with earlier studies of the kinetics of calcite nucleation by the *S. leopoliensis* PCC 7942 which indicated that calcite nucleation was independent of photosynthesis and active ion transport mechanisms across the cell membrane, but rather related to the surface properties of the cells which facilitated calcite nucleation by reducing the interfacial free energy of the calcite nuclei (Obst et al., in press).

The effective thickness of the aragonite-like $CaCO_3$ layer surrounding the bacteria was larger at the time of the onset, but almost negligible after calcite precipitation took place (Fig. 6e–h). This supports the idea that the amorphous aragonite-like $CaCO_3$ that formed within the EPS of *S. leopoliensis* PCC 7942 is a metastable phase which rapidly dissolves once the solution is undersaturated with respect to aragonite but in equilibrium with calcite.

Whereas it has been reported that almost all biogenic ACC deposits have significant amounts of magnesium or phosphorous incorporated (Weiner et al., 2003), our experimental results, which use synthetic solutions of $CaCl_2$ and $NaHCO_3$ without magnesium and phosphates, indicate that ACC can be efficiently stabilized by purely organic biomacromolecules.

4.4. Bacterially influenced precipitation of amorphous, aragonite-like $CaCO_3$ as a protection mechanism against calcite formation

Although these results show unambiguously that *S. leopoliensis* PCC 7942 strongly influences the nucleation of $CaCO_3$, the evolutionary benefit for the cyanobacteria remains unclear. From a thermodynamic point of view the precipitation of calcite is favored as it is the most stable polymorph of $CaCO_3$. However, from the bacteria's perspective the formation of large calcite crystals attached to the cell envelope is unfavorable. The crystals would cause the cells to lose their buoyancy and thus gravity would remove them from the euphotic zone in their natural environment. Natural environments such as lakes and rivers, where planktonic cyanobacteria occur and limestone is abundant in the catchment areas, are often supersaturated with respect to $CaCO_3$ in summertime. Carbonate precipitation in so-called whiting events has often been observed during blooms of cyanobacteria, and particularly in oligotrophic environments where they often dominate the primary production (Thompson et al., 1997). These authors also state that these whiting events are responsible for the formation of most of the <5 μm sized suspended carbonate sediments in alkaline lake and marine environments, where the mineralogy is different because of the high Mg:Ca ratios of ~5 in seawater. The bacterial cell wall is negatively charged and often collects essential ions such as Ca^{2+} and Mg^{2+} or immobilizes toxic ions such as Hg^{2+}, Cu^{2+} or Cd^{2+} and prevents them from entering the cells (Beveridge, 1988). At the same time, the attraction of bivalent ions increases supersaturation with respect to mineral phases and therefore the risk of potentially fatal uncontrolled growth of precipitates on the cell surface. This is of particular importance for the photoautotrophic cyanobacteria which take up CO_2 or HCO_3^- ions and therefore increase the carbonate concentration in their local environment. This micro- or submicro-environment is diffusion controlled (Beveridge,

1988). Therefore the cyanobacteria might use a strategy which helps avoid the nucleation of carbonate crystals attached to their surface which might grow independent of any bacterial control.

We postulate that the controlled precipitation of an amorphous $CaCO_3$ layer within the EPS surrounding a cell would be an efficient strategy for lowering the supersaturation of the surrounding bulk water in order to avoid the lethal effects of calcite precipitation on the cell surface. By initiating the formation of an amorphous aragonite-like $CaCO_3$ phase which covers the whole cell surface, the cyanobacteria prevent the nucleation of calcite which is the most stable and therefore least reactive form of $CaCO_3$. This is so because a direct phase transition from this amorphous aragonite-like $CaCO_3$ to calcite is blocked by a large activation energy barrier (Xu et al., 2008). Therefore the controlled precipitation of an amorphous aragonite-like $CaCO_3$ layer offers the bacteria the advantage of acting as a temporary Ca-buffer. For short periods of high supersaturation the amorphous layer of aragonite-like $CaCO_3$ stores the excess-Ca which contributes to the supersaturation. However, it dissolves more rapidly once the ion activity product falls below aragonite saturation due to changes in the environment such as the diurnal pH cycle due to photosynthesis (Eiler et al., 2006) or seasonal cycles like seasonal precipitation events (Teranes et al., 1999) or mixing of a lake, even if the water is still saturated with respect to calcite. This precipitation mechanism seemed to be strongly influenced by the EPS and could eventually fall into the category of biological control according to the definition provided by Lowenstam and Weiner (1989).

The proposed protection mechanisms of the cyanobacteria seemed to be less important in the experiments conducted with cells harvested at the end of the stationary phase. No significant amounts of aragonite-like $CaCO_3$ were formed within the EPS of cells at a stage when they were no longer viable (Fig. 6i–o). However at the same time the amount of Ca adsorbed to the surface of the bacteria was much smaller compared to more viable cells from the exponential phase (Fig. 6a–d). Based on these results we hypothesize that the EPS at this stage of growth contains smaller amounts of negatively charged sites such as carboxylic groups. A possible explanation might be a slower metabolism which reduces the amounts of bivalent cations needed by the cyanobacteria at this stage of growth.

This theory of a protection mechanism against calcite precipitation on the cell surface might provide an efficient protection to overcome short periods of supersaturation. Schultze-Lam et al. (1992) suggested an alternative, based on TEM studies of another *Synechococcus* strain wherein they observed the precipitation of small grained gypsum and calcite crystals on a proteinaceous S-layer which surrounded the investigated strain. The authors hypothesized that the bacteria could strip off this S-layer with the attached precipitates once they become too thick, and the bacteria could use this as a protection mechanism against encrustation. The two mechanisms do not contradict each other and might coexist. However, in previous studies (Obst and Dittrich, 2005; Obst et al., 2006) no S-layer was observed on the surface of the strain *S. leopoliensis* PCC 7942.

4.5. X-ray amorphous $CaCO_3$ and its significance in bacterial calcification

In contrast to eukaryotes, the involvement of an amorphous phase in the precipitation of $CaCO_3$ by cyanobacteria and the precipitation of different minerals by the same species have rarely been reported (Lowenstam and Weiner, 1989). This is most likely related to the fact that microbially mediated amorphous precipitates are very difficult to detect because of their low abundance. Golubic and Campbell (1981) speculated about the formation of aragonitic granules by marine cyanobacteria of the genus *Rivularia* via the deposition of an amorphous $CaCO_3$ phase. This amorphous phase was postulated as a precursor for the subsequent precipitation of acicular aragonite crystals which they confirmed by XRD measurements. Their suggestion of an intermediate amorphous $CaCO_3$ phase was based on the surface morphology observed by SEM, not on XRD measurements. This is one of only a few cases reported where one bacterial species is involved in the formation of two different mineral phases (Lowenstam, 1986). Few other cases report the presence of amorphous $CaCO_3$ phases in microbially mediated biomineralization. Benzerara et al. (2003) reported the precipitation of an ACC phase surrounding needle-like calcite nanocrystals and Benzerara et al. (2006) observed an ACC phase in microbialites. In both cases the observations were interpreted as the result of biomineralization in organic matrices, which is in full agreement with our observations and interpretations.

According to Addadi et al. (2003) in the process of biomineral nucleation the short-range order of amorphous phases is believed to be genetically controlled by the biomineralizing organism. However, their hypothesis was based on biominerals formed by eukaryotes only. In our study we found evidence that the nucleation rate is influenced by supersaturation with respect to the mineral phase and the microbial response to nutrient conditions but our method does not allow conclusions regarding genetic control over the $CaCO_3$ polymorph. Thus, our results do not contradict the hypothesis of (Addadi et al., 2003), but they indicate at least that the microbial precipitation of a specific $CaCO_3$ polymorph is not solely under genetic control but can also be a response to environmental conditions.

4.6. Model of $CaCO_3$ nucleation on the cyanobacteria

Based on the data reported above a model of the temporal and spatial evolution of calcite precipitation mediated by cyanobacteria of the strain *S. leopoliensis* PCC 7942 was developed. Based on the result that a fraction of the EPS can easily be stripped off the cells (e.g. by shear stress) whereas another fraction of the EPS remain on the surface (e.g. Fig. 3a), this model assumes a two-layer structure of EPS. The bacterial cell is surrounded by a thin layer of EPS which is closely bound to the cell surface forming a capsular-like structure (Fig. 7a). The cell including the closely bound EPS, is embedded in a second layer of loosely bound EPS. This model is similar to structures that Eboigbodin and Biggs (2008) described for an *E. coli* strain as Free-EPS and Bound-EPS. Bellezza and Albertano (2006)

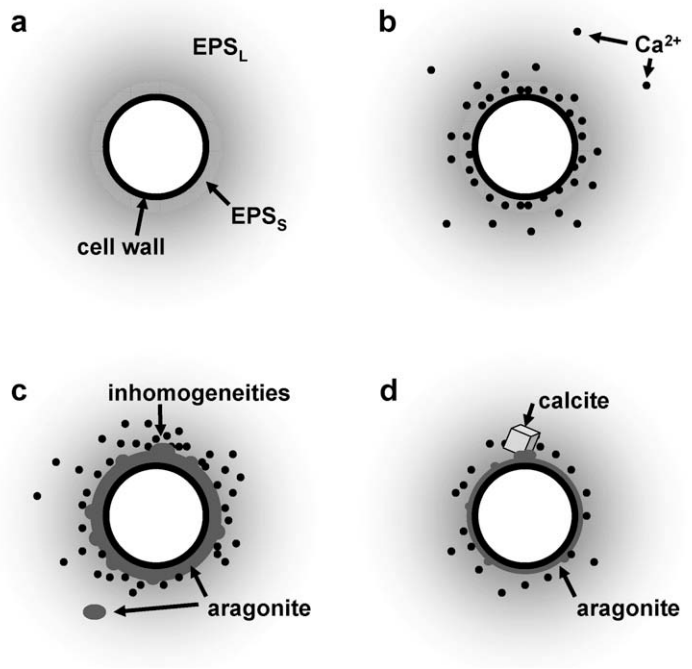

Fig. 7. Schematic outlining proposed model of the temporal evolution of calcite nucleation on the surface of *S. leopoliensis* PCC 7942. (a) The cell is surrounded by a layer of closely bound, capsular like EPS, which is embedded in a matrix of loosely bound polymers. (b) Ca^{2+} ions are adsorbed to the EPS, preferentially to the closely bound type (EPS_s). (c) Aragonite-like $CaCO_3$ is nucleated very close to the cell surface within the closely bound polymer. The induction time of this rather homogeneous process is shorter than the induction time of calcite nucleation. (d) Once calcite nucleates and starts precipitating, the aragonite-like $CaCO_3$ is no longer stable and dissolves.

also characterized two different types of EPS which reacted differently when they stained polysaccharides in their studies of the two cyanobacterial strains *Scytonema ocellatum* CP8-2 and *Fischerella maior* NAV 10 bis. In their study they analyzed the structure of these layers and described them as a compact and a diffuse layer of extracellular polymers.

In our model Ca^{2+} ions adsorb onto both layers of EPS. After a period of time, which is likely significantly shorter than the induction time t_i of calcite nucleation ($t_i = 45$ h for the six-times saturated solution, $t_i = 12$ h for the 9.3 times saturated solution, respectively), the amorphous aragonite-like $CaCO_3$ nucleates starting within the closely bound EPS layer close to the cell membrane (Fig. 7b). The precipitation of aragonite-like $CaCO_3$ continues throughout the closely bound EPS layer, which is not perfectly homogeneous (Fig. 7c). This process occurs on the vast majority of all cyanobacterial cells in a rather homogeneous fashion. Calcite eventually nucleates on a small fraction of the cells. The onset of the calcite nucleation is subsequent to the much faster nucleation of aragonite-like $CaCO_3$ (Fig. 7d). Once calcite has nucleated, the precipitation of the thermodynamically most stable polymorph of $CaCO_3$ continues unless the solution is no longer supersaturated with respect to calcite. At this stage the previously precipitated aragonite-like $CaCO_3$ is not stable and dissolves once the solution becomes undersaturated with respect to aragonite (Fig. 7d). Therefore the time period wherein aragonite-like $CaCO_3$ can be detected is relatively short (i.e. hours to a few days). In addition to these temporal constraints, this phenomenon is difficult to detect due to the lack of long-range order and the small size of the ACC-layer. So far, STXM has been the only technique capable of detecting and characterizing this phase.

Similar two stage processes of cation adsorption and nucleation of a mineral phase on the cell surface or within extracellular polymers followed by a second stage of precipitation independently of biogenic influence have been reported previously for example by Konhauser (1998) for Fe-mineralizing bacteria and by Schultze-Lam and Beveridge (1994) for cyanobacterial sulfate and carbonate precipitation.

5. CONCLUSION

At least two different and subsequent mechanisms of $CaCO_3$ precipitation play an important role in the calcification of photoautotrophic planktonic cyanobacteria of the strain *S. leopoliensis* PCC 7942:

(i) The bacterially influenced precipitation of an X-ray amorphous $CaCO_3$ layer within the extracellular polymers of the cyanobacteria which is very homogeneous throughout the population, and
(ii) the subsequent precipitation of crystalline calcite which is initiated by the cells, but lacks bacterial control.

Soft X-ray spectromicroscopy showed an aragonite-like short-range order within the amorphous $CaCO_3$. From

these results we conclude that the precipitation of aragonite-like $CaCO_3$ is a mechanism by which the cyanobacteria successfully avoids uncontrolled and potentially lethal precipitation of the thermodynamically more stable calcite on their surface. The latter precipitation would inescapably occur in waters supersaturated with respect to calcite but lacking inhibitors of calcite precipitation such as Mg^{2+} in seawater. The controlled precipitation of aragonite-like $CaCO_3$ is reversible once the supersaturation drops, e.g. due to diurnal or seasonal cycles or the abiotic precipitation of calcite. This mechanism, which is only maintained as long as the cells are viable, enables the population of cyanobacteria to overcome periods of $CaCO_3$ supersaturation which naturally occur in their environments.

ACKNOWLEDGMENTS

We thank P. Gasser (EMEZ, ETHZ), and L. Holzer (3D-Mat, EMPA) for expert sample preparation by focused ion beam milling. We furthermore thank Mary Liang, University of Alberta, Edmonton, Physics Department for her help with the electron diffraction experiments and Tom Bonli, University of Saskatchewan, Saskatoon, Geology Department for his help on the XRD measurements. We also thank Drs. H.P. Schwarz and J. Rink (School of Geography and Earth Sciences, McMaster) for providing samples of calcite and aragonite. We thank Drew Bertwistle (CLS) and David Kilcoyne (ALS) for their support of the respective beamlines and STXMs. Finally, we would like to thank Kurt Konhauser and two anonymous reviewers for their detailed comments that were of great help for improving the quality of this manuscript. This study was supported by the Swiss National Science Foundation (PBEZ2-115172), NSERC, Canada Research Chair. The CLS is supported by NSERC, CIHR, NRC and the University of Saskatchewan. The ALS is supported by the Office of Basic Energy Sciences of the US Department of Energy.

APPENDIX A. SUPPLEMENTARY DATA

Supplementary data associated with this article can be found, in the online version, at doi:10.1016/j.gca.2009.04.013.

REFERENCES

Addadi L., Raz S. and Weiner S. (2003) Taking advantage of disorder: amorphous calcium carbonate and its roles in biomineralization. *Adv. Mater.* **15**(12), 959–970.

Arp G., Reimer A. and Reitner J. (2001) Photosynthesis-induced biofilm calcification and calcium concentrations in phanerozoic oceans. *Science* **292**(5522), 1701–1704.

Barthelmy D. (2000) Available from: www.webmineral.com, vol. 2008.

Becker A., Bismayer U., Epple M., Fabritius H., Hasse B., Shi J. M. and Ziegler A. (2003) Structural characterisation of X-ray amorphous calcium carbonate (ACC) in sternal deposits of the crustacea *Porcellio scaber*. *Dalton Trans.*(4), 551–555.

Bellezza S. and Albertano P. (2006) Exopolysaccharides of two cyanobacterial strains from Roman hypogea. *Geomicrobiol. J.* **23**(5), 301–310.

Benzerara K., Menguy N., Guyot F., Dominici C. and Gillet P. (2003) Nanobacteria-like calcite single crystals at the surface of the *Tataouine meteorite*. *Proc. Natl. Acad. Sci. USA* **100**(13), 7438–7442.

Benzerara K., Menguy N., Guyot F., Skouri F., de Luca G., Barakat M. and Heulin T. (2004a) Biologically controlled precipitation of calcium phosphate by *Ramlibacter tataouinensis*. *Earth Planet. Sci. Lett.* **228**(3–4), 439–449.

Benzerara K., Menguy N., Lopez-Garcia P., Yoon T. H., Kazmierczak J., Tyliszczak T., Guyot F. and Brown G. E. (2006) Nanoscale detection of organic signatures in carbonate microbialites. *Proc. Natl. Acad. Sci. USA* **103**(25), 9440–9445.

Benzerara K., Yoon T. H., Tyliszczak T., Constantz B., Spormann A. M. and Brown G. E. (2004b) Scanning transmission X-ray microscopy study of microbial calcification. *Geobiology* **2**(4), 249–259.

Beveridge T. J. (1988) The bacterial surface – general considerations towards design and function. *Can. J. Microbiol.* **34**(4), 363–372.

Bluhm H., Andersson K., Araki T., Benzerara K., Brown G. E., Dynes J. J., Ghosal S., Gilles M. K., Hansen H. C., Hemminger J. C., Hitchcock A. P., Ketteler G., Kilcoyne A. L. D., Kneedler E., Lawrence J. R., Leppard G. G., Majzlam J., Mun B. S., Myneni S. C. B., Nilsson A., Ogasawara H., Ogletree D. F., Pecher K., Salmeron M., Shuh D. K., Tonner B., Tyliszczak T., Warwick T. and Yoon T. H. (2006) Soft X-ray microscopy and spectroscopy at the molecular environmental science beamline at the advanced light source. *J. Electron Spectrosc. Relat. Phenomena* **150**(2–3), 86–104.

Bosak T. and Newman D. K. (2005) Microbial kinetic controls on calcite morphology in supersaturated solutions. *J. Sedimentary Res.* **75**(2), 190–199.

Braissant O., Cailleau G., Dupraz C. and Verrecchia A. P. (2003) Bacterially induced mineralization of calcium carbonate in terrestrial environments: the role of exopolysaccharides and amino acids. *J. Sedimentary Res.* **73**(3), 485–490.

Braissant O., Decho A. W., Dupraz C., Glunk C., Przekop K. M. and Visscher P. T. (2007) Exopolymeric substances of sulfate-reducing bacteria: interactions with calcium at alkaline pH and implication for formation of carbonate minerals. *Geobiology* **5**(4), 401–411.

de Groot F. (2005) Multiplet effects in X-ray spectroscopy. *Coordination Chem. Rev.* **249**(1–2), 31–63.

de Groot F. M. F., Fuggle J. C., Thole B. T. and Sawatzky G. A. (1990) 2p X-ray absorption of 3d transition-metal compounds – an atomic multiplet description including the crystal field. *Phys. Rev. B* **42**(9), 5459–5468.

De Yoreo J. J. and Vekilov P. G. (2003) Principles of crystal nucleation and growth. In *Biomineralization*, vol. 54, pp. 57–93. Biomineralization. Mineralogical Soc America.

Dove P. M. and Hochella M. F. (1993) Calcite precipitation mechanisms and inhibition by orthophosphate – in situ observations by scanning force microscopy. *Geochim. Cosmochim. Acta* **57**(3), 705–714.

Doyle C. S., Kendelewicz T. and Brown G. E. (2004) Inhibition of the reduction of Cr(VI) at the magnetite–water interface by calcium carbonate coatings. *Appl. Surf. Sci.* **230**(1–4), 260–271.

Dynes J. J., Lawrence J. R., Korber D. R., Swerhone G. D. W., Leppard G. G. and Hitchcock A. P. (2006a) Quantitative mapping of chlorhexidine in natural river biofilms. *Sci. Total Environ.* **369**(1–3), 369–383.

Dynes J. J., Tyliszczak T., Araki T., Lawrence J. R., Swerhone G. D. W., Leppard G. G. and Hitchcock A. P. (2006b) Speciation and quantitative mapping of metal species in microbial biofilms using scanning transmission X-ray microscopy. *Environ. Sci. Technol.* **40**(5), 1556–1565.

Eboigbodin K. E. and Biggs C. A. (2008) Characterization of the extracellular polymeric substances produced by *Escherichia coli* using infrared spectroscopic, proteomic, and aggregation studies. *Biomacromolecules* **9**(2), 686–695.

Eiler A., Olsson J. A. and Bertilsson S. (2006) Diurnal variations in the auto- and heterotrophic activity of cyanobacterial phycospheres (*Gloeotrichia echinulata*) and the identity of attached bacteria. *Freshwater Biol.* **51**(2), 298–311.

Erez J. (2003) The source of ions for biomineralization in foraminifera and their implications for paleoceanographic proxies. In *Biomineralization*, vol. 54, pp. 115–149. Biomineralization. Mineralogical Soc America.

Golubic S. (1973) The relationship between blue-green algae and carbonate deposits. In *The Biology of Blue-Green Algae*, vol. 9 (eds. N. G. Carr and B. A. Whitton). Blackwell Scientific Publications, pp. 434–472.

Golubic S. and Campbell S. E. (1981) Biogenically formed aragonite congretions in marine *Rivularia*. In *Phanerozoic Stromatolites* (ed. C. Monty). Springer, pp. 220–229.

Hartley A. M., House W. A., Callow M. E. and Leadbeater B. S. C. (1995) The role of a green-alga in the precipitation of calcite and the coprecipitation of phosphate in fresh-water. *Int. Revue der gesamten Hydrobiol.* **80**(3), 385–401.

Henke B. L., Gullikson E. M. and Davis J. C. (1993) X-ray interactions – photoabsorption, scattering, transmission, and reflection at $E = 50 - 30{,}000$ eV, $Z = 1 - 92$. *Atomic Data Nucl. Data Tables* **54**(2), 181–342.

Himpsel F. J., Karlsson U. O., McLean A. B., Terminello L. J., Degroot F. M. F., Abbate M., Fuggle J. C., Yarmoff J. A., Thole B. T. and Sawatzky G. A. (1991) Fine-structure of the Ca 2p X-ray-absorption edge for bulk compounds, surfaces, and interfaces. *Phys. Rev. B* **43**(9), 6899–6907.

Hitchcock A. P. (2008) aXis2000 is written in Interactive Data Language (IDL). It is available free for non-commercial use from <http://unicorn.mcmaster.ca/aXis2000.html/>.

Hitchcock A. P., Dynes J. J., Johansson G., Wang J. and Botton G. (2008) Comparison of NEXAFS microscopy and TEM-EELS for studies of soft matter. *Micron* **39**(3), 311–319.

Hunter R. C., Hitchcock A. P., Dynes J. J., Obst M. and Beveridge T. J. (2008) Mapping the speciation of iron minerals in *Pseudomonas aeruginosa* biofilms using scanning transmission X-ray microscopy. *Geochim. Cosmochim. Acta* **42**(23), 8766–8772.

Kah L. C. and Riding R. (2007) Mesoproterozoic carbon dioxide levels inferred from calcified cyanobacteria. *Geology* **35**(9), 799–802.

Kawaguchi T. and Decho A. W. (2002) A laboratory investigation of cyanobacterial extracellular polymeric secretions (EPS) in influencing $CaCO_3$ polymorphism. *J. Crystal Growth* **240**(1–2), 230–235.

Kaznatcheev K. V., Karunakaran C., Lanke U. D., Urquhart S. G., Obst M. and Hitchcock A. P. (2007) Soft X-ray spectromicroscopy beamline at the CLS: commissioning results. *Nucl. Instrum. Methods Phys. Res. A Accelerators Spectrometers Detectors Assoc. Equipment* **582**(1), 96–99.

Kilcoyne A. L. D., Tyliszczak T., Steele W. F., Fakra S., Hitchcock P., Franck K., Anderson E., Harteneck B., Rightor E. G., Mitchell G. E., Hitchcock A. P., Yang L., Warwick T. and Ade H. (2003) Interferometer-controlled scanning transmission X-ray microscopes at the advanced light source. *J. Synchrotron Radiat.* **10**, 125–136.

Konhauser K. O. (1998) Diversity of bacterial iron mineralization. *Earth-Sci. Rev.* **43**(3–4), 91–121.

Koprinarov I. N., Hitchcock A. P., McCrory C. T. and Childs R. F. (2002) Quantitative mapping of structured polymeric systems using singular value decomposition analysis of soft X-ray images. *J. Phys. Chem. B* **106**(21), 5358–5364.

Kralj D., Brecevic L. and Nielsen A. E. (1994) Vaterite growth and dissolution in aqueous-solution 2. *Kinet. Dissolution J. Crystal Growth* **143**(3–4), 269–276.

Küchler-Krischun J. and Kleiner J. (1990) Heterogeneously nucleated calcite precipitation in lake constance – a short-time resolution study. *Aquat. Sci.* **52**(2), 176–197.

Lam R. S. K., Charnock J. M., Lennie A. and Meldrum F. C. (2007) Synthesis-dependant structural variations in amorphous calcium carbonate. *CrystEngComm* **9**(12), 1226–1236.

Lebron I. and Suarez D. L. (1998) Kinetics and mechanisms of precipitation of calcite as affected by P-CO_2 and organic ligands at 25 degrees C. *Geochim. Cosmochim. Acta* **62**(3), 405–416.

Lee M. R., Brown D. J., Smith C. L., Hodson M. E., Mackenzie M. and Hellmann R. (2007) Characterization of mineral surfaces using FIB and TEM: a case study of naturally weathered alkali feldspars. *Am. Mineral.* **92**(8–9), 1383–1394.

Lerotic M., Jacobsen C., Schafer T. and Vogt S. (2004) Cluster analysis of soft X-ray spectromicroscopy data. *Ultramicroscopy* **100**(1–2), 35–57.

Lopez-Garcia P., Kazmierczak J., Benzerara K., Kempe S., Guyot F. and Moreira D. (2005) Bacterial diversity and carbonate precipitation in the giant microbialites from the highly alkaline Lake Van, Turkey. *Extremophiles* **9**(4), 263–274.

Lowenstam H. A. (1986) Mineralization processes in monerans and protoctists. In *Biomineralization in Lower Plants and Animals Proceedings of an International Symposium, Birmingham, April (15–19), 1985*, vol. 401 (eds. B. S. C. Leadbeater and R. Riding). Clarendon Press, p. XII.

Lowenstam H. A. and Weiner S. (1989) *On Biomineralization*. Oxford University Press.

Martinez R. E., Pokrovsky O. S., Schott J. and Oelkers E. H. (2008) Surface charge and zeta-potential of metabolically active and dead cyanobacteria. *J. Colloid Interface Sci.* **323**(2), 317–325.

Merz-Preiss M. (2000) Calcification in cyanobacteria. In *Microbial Sediments* (eds. R. E. Riding and S. M. Awramik). Springer-Verlag/Heidelberg, Berlin/New York, pp. 50–56.

Merz M. U. E. (1992) The biology of carbonate precipitation by cyanobacteria. *Facies* **26**, 81–101.

Metzler R. A., Abrecht M., Olabisi R. M., Ariosa D., Johnson C. J., Frazer B. H., Coppersmith S. N. and Gilbert P. (2007) Architecture of columnar nacre, and implications for its formation mechanism. *Phys. Rev. Lett.* **98**(26).

Naftel S. J., Sham T. K., Yiu Y. M. and Yates B. W. (2001) Calcium L-edge XANES study of some calcium compounds. *J. Synchrotron Radiat.* **8**, 255–257.

Neu T. R. and Lawrence J. R. (2005) One-photon versus two-photon laser scanning microscopy and digital image analysis of microbial biofilms. In *Microbial Imaging*, vol. 34 (eds. S. T. T and P. C. C). Elsevier Academic Press Inc., pp. 89–136.

Obst M. and Dittrich M. (2005) Living under an atomic force microscope – an optimized approach for in vivo investigations on surface alterations towards biomineral nucleation on cyanobacterial cells. *Geobiology* **3**(3), 179–193.

Obst M., Dittrich M. and Kuehn H. (2006) Calcium adsorption and changes of the surface microtopography of cyanobacteria studied by AFM, CFM, and TEM with respect to biogenic calcite nucleation. *Geochem. Geophys. Geosyst.*, 7.

Obst M., Gasser P., Mavrocordatos D. and Dittrich M. (2005) TEM-specimen preparation of cell/mineral interfaces by focused ion beam milling. *Am. Mineral.* **90**(8–9), 1270–1277.

Obst M., Wehrli B. and Dittrich M. (in press) $CaCO_3$ nucleation by Cyanobacteria – laboratory evidence for a passive, surface-induced mechanism. Geobiology.

Pentecost A. (1991) Calcification processes in algae and cyanobacteria. In *Calcareous Algae and Stromatolites* (ed. R. Riding). Springer, pp. 3–20.

Plummer L. N. and Busenberg E. (1982) The solubilities of calcite, aragonite and vaterite in CO_2–H_2O solutions between 0-

degrees-C and 90-degrees-C, and an evaluation of the aqueous model for the system $CaCO_3$–CO_2–H2O. *Geochim. Cosmochim. Acta* **46**(6), 1011–1040.

Politi Y., Mahamid J., Goldberg H., Weiner S. and Addadi L. (2007) Asprich mollusk shell protein: in vitro experiments aimed at elucidating function in $CaCO_3$ crystallization. *CrystEngComm* **9**(12), 1171–1177.

Riding R. (1992) Temporal variation in calcification in marine cyanobacteria. *J. Geol. Soc.* **149**, 979–989.

Rodriguez-Blanco J. D., Shaw S. and Benning L. G. (2008) How to make 'stable' ACC: protocol and preliminary structural characterization. *Mineral. Mag.* **72**(1), 283–286.

Rodriguez-Navarro C., Rodriguez-Gallego M., Ben Chekroun K. and Gonzalez-Munoz M. T. (2003) Conservation of ornamental stone by *Myxococcus xanthus*-induced carbonate biomineralization. *Appl. Environ. Microbiol.* **69**(4), 2182–2193.

Schultze-Lam S. and Beveridge T. J. (1994) Nucleation of celestite and strontianite on a cyanobacterial S- layer. *Appl. Environ. Microbiol.* **60**(2), 447–453.

Schultze-Lam S., Harauz G. and Beveridge T. J. (1992) Participation of a cyanobacterial-S layer in fine-grain mineral formation. *J. Bacteriol.* **174**(24), 7971–7981.

Stoehr J. (1996) *NEXAFS Spectroscopy*. Springer.

Teranes J. L., McKenzie J. A., Bernasconi S. M., Lotter A. F. and Sturm M. (1999) A study of oxygen isotopic fractionation during bio-induced calcite precipitation in eutrophic Baldeggersee, Switzerland. *Geochim. Cosmochim. Acta* **63**(13–14), 1981–1989.

Thompson J. B. and Ferris F. G. (1990) Cyanobacterial precipitation of gypsum, calcite, and magnesite from natural alkaline lake water. *Geology* **18**(10), 995–998.

Thompson J. B., Schultze-Lam S., Beveridge T. J. and DesMarais D. J. (1997) Whiting events: biogenic origin due to the photosynthetic activity of cyanobacterial picoplankton. *Limnol. Oceanogr.* **42**(1), 133–141.

Weiner S., Levi-Kalisman Y., Raz S. and Addadi L. (2003) Biologically formed amorphous calcium carbonate. *Connect. Tissue Res.* **44**, 214–218.

Weisse T. (1993) Dynamics of autotrophic picoplankton in marine and freshwater ecosystems. In *Advances in Microbial Ecology*, vol. 13 (ed. J. G. Jones). Plenum Press, pp. 327–370.

Xu A. W., Dong W. F., Antonietti M. and Colfen H. (2008) Polymorph switching of calcium carbonate crystals by polymer-controlled crystallization. *Adv. Funct. Mater.* **18**(8), 1307–1313.

Young J. R., Davis S. A., Bown P. R. and Mann S. (1999) Coccolith ultrastructure and biomineralisation. *J. Struct. Biol.* **126**(3), 195–215.

Zhang Y. P. and Dawe R. A. (2000) Influence of Mg^{2+} on the kinetics of calcite precipitation and calcite crystal morphology. *Chem. Geol.* **163**(1–4), 129–138.

Zuddas P. and Mucci A. (1994) Kinetics of calcite precipitation from seawater.1. A classical chemical-kinetics description for strong electrolyte-Solutions. *Geochim. Cosmochim. Acta* **58**(20), 4353–4362.

Zuddas P., Pachana K. and Faivre D. (2003) The influence of dissolved humic acids on the kinetics of calcite precipitation from seawater solutions. *Chem. Geol.* **201**(1–2), 91–101.

Associate editor: Peggy A. O'Day